Exchange splitting and exchange-induced nonreciprocal photonic behavior of graphene in CrI_3-graphene van der Waals heterostructures

Alexander M. Holmes [1,*] Samaneh Pakniyat [1,†] S. Ali Hassani Gangaraj,[2,‡] Francesco Monticone [2,§] Michael Weinert,[3,‖] and George W. Hanson [1,¶]

[1]*Department of Electrical Engineering, University of Wisconsin-Milwaukee, 3200 N. Cramer St., Milwaukee, Wisconsin 53211, USA*

[2]*School of Electrical and Computer Engineering, Cornell University, Ithaca, New York 14853, USA*

[3]*Department of Physics, University of Wisconsin-Milwaukee, Milwaukee, Wisconsin, 53211, USA*

(Received 26 May 2020; accepted 6 August 2020; published 20 August 2020)

The exchange splitting and resulting electromagnetic response of graphene in a monolayer chromium triiodide (CrI_3)–graphene van der Waals heterostructure are considered using a combination of density-functional theory and electromagnetic calculations. Although the effective exchange fields are in the hundreds of Tesla, for the equilibrium separation nonreciprocal effects are found to be weak compared to those for a comparable external magnetic bias. For nonequilibrium separations, nonreciprocal effects can be substantial.

DOI: 10.1103/PhysRevB.102.075435

I. INTRODUCTION

Graphite consists of parallel atomic layers of carbon atoms, the layers being weakly bound together by van der Waals (vdW) forces. As such, graphite is easily cleaved to form few layer materials, or even monolayers (graphene). Since its experimental isolation in 2004 [1], graphene has been an object of considerable study for both scientific and industrial investigators. Graphene's most notable feature is its atomic hexagonal lattice, which results in linear electronic dispersion and the presence of Dirac points at the Fermi level. As a result, electrons behave as massless particles in the vicinity of the Dirac point, leading to extraordinary electrical and mechanical properties [2].

Bulk chromium triiodide, CrI_3, also is a layered vdW material that can be easily cleaved, and is relatively stable in ambient conditions [3]. Bulk CrI_3 is a ferromagnetic (FM) insulator with a relatively high Curie temperature of $T_c = 61$ K [3]. The two-dimensional (2D)/monolayer form of CrI_3 consists of Cr^{3+} ions and I^- ions that form edge-sharing octahedra arranged in a hexagonal honeycomb lattice with an approximate thickness of 0.6 nm. Like its bulk form, monolayer CrI_3 is also a FM insulator, with an out-of-plane easy axis and somewhat reduced T_c of 45 K [4].

The controlled growth/deposition of 2D materials can lead to vdW heterostructures that result in exceedingly thin structures with enhanced functionality. Here, we exploit the proximity exchange between a 2D ferromagnet and graphene. In its monolayer form, CrI_3 exhibits massive local Cr magnetic moments of $3\mu_B$, which potentially can induce large exchange splittings in adjacent layers of a heterostructure. Since 2D CrI_3 has a hexagonal structure, it is well lattice-matched with graphene. Magnetic order in CrI_3 has been studied experimentally in [4–8], and in other 2D magnets, such as $MnSe_2$ [9,10] and $CrGeTe_3$ [11,12]. In all cases, these 2D magnets have out of the plane magnetization. In some cases, magnetic effects can be controlled via electrostatic gating [7,8], or strain [13,14].

Enormous pseudomagnetic fields (on the order of hundreds of Tesla) and associated pseudo-Landau levels (LLs) have been predicted in strained systems [15]. Such fields do not break time-reversal (TR) symmetry, and cannot lead to nonreciprocal behavior. Importantly, the exchanged-induced fields described here do break TR: The effective Hamiltonians for both an external magnetic field and a ferro-/antiferromagnetic system contain terms that explicitly couple to the spin that are not invariant under time reversal; in contrast, the pseudomagnetic fields in strained graphene couple to charge only, and hence preserve time-reversal symmetry. Exchange interactions in similar vdW heterostructures have been considered, e.g., $Cr_2Ge_2Te_6$-graphene [16], where equilibrium exchange splittings were calculated to be approximately 5 meV, and EuS-graphene [17]. A Chern insulating state can be realized in graphene in proximity to CrI_3, via the magnetic exchange field and Rashba spin-orbit coupling [14,18]. However, to achieve this, the heterostructure needs to be compressed from its equilibrium state which increases the effective field [18].

In this work, we use first-principles density functional theory (DFT) calculations to show that the proximity exchange in graphene due to monolayer CrI_3 can result in an enormous exchange field, and then we investigate the conductivity of graphene due to the CrI_3 exchange field, and the behavior of bulk and nonreciprocal edge surface-plasmon polaritons (SPPs). A comparison is made with the conductivity and SPP properties of graphene in an external magnetic field, and significant differences are found in the two cases. We also examine Faraday rotation (FR) of graphene [19,20]. In Ref. [21] the graphene CrI_3 interface is also investigated using

*holmesam@uwm.edu
†pakniyat@uwm.edu
‡ali.gangaraj@gmail.com
§francesco.monticone@cornell.edu
‖weinert@uwm.edu
¶george@uwm.edu

DFT, and in Ref. [22] surface polaritons on graphene coupled to a bulk antiferromagnetic insulator were considered.

The principal findings of this work are (1) the equilibrium (minimum energy) separation between the CrI_3 and graphene is approximately 3.75 Å, at which point the exchange splitting is 21 meV, corresponding to an effective exchange field of 100 T and a chemical potential of $\mu = -0.3\,\text{eV}$, which self-biases the graphene. Referring to graphene's conductivity in the CrI_3-graphene heterostructure, (2) LLs, which are the most prominent feature of the graphene conductivity in a strong external field, are absent in the case of the exchange field. (3) In the far-infrared considered here, the intraband conductivity is dominant, with diagonal element values that are approximately the same as isolated graphene with no applied magnetic bias and $\mu = -0.3\,\text{eV}$, whereas the off-diagonal elements are similar in magnitude to those in the external bias case. (4) Because of the large diagonal conductivity response compared to having an external bias (in which case most of the Drude weight is transferred to the Landau levels), the resulting nonreciprocity due to the exchange field is considerably less then for an external magnetic field of the same strength. For smaller separation (achievable through, e.g., strain), nonreciprocal effects in Faraday rotation are still rather modest, but a unidirectional edge SPP can be found.

The article is organized as follows. In Sec. II the density functional calculations are presented, and results for exchange splittings and the corresponding effective exchange fields are given. In Sec. III the exchange-field-induced graphene conductivity is discussed, and compared with that arising from an external bias, and bulk and edge surface plasmons are considered. The edge SPPs for the exchange field are slightly nonreciprocal for the equilibrium separation, whereas for the external bias case they are highly nonreciprocal (unidirectional), tightly confined, long-lasting, and robust to material discontinuities. In Sec. IV, FR is shown for both the exchange and external bias fields, where, again, the exchange field is shown to produce modest FR. The Supplemental Material [23] contains further results from the DFT calculations, and the derivation of the edge plasmon dispersion. In the following, the suppressed time dependence is $e^{-i\omega t}$.

II. DENSITY FUNCTIONAL CALCULATIONS

Density functional calculations for graphene on CrI_3 have been reported previously, [14], with an emphasis on the topological aspects of the compressed system. Here the focus is on the effect of the induced exchange field on the graphene electronic structure, and the implications for the calculation of optical properties discussed later; detailed first-principles calculations of the optical properties of the CrI_3 itself have also been reported previously [29].

To model the composite system, we consider 5×5 graphene on a free-standing $\sqrt{3} \times \sqrt{3}$ CrI_3 monolayer, Fig. 1(a), which has a small lattice mismatch of ~1%. (Additional calculations for $\sqrt{31} \times \sqrt{31}$ graphene on $2 \times 2CrI_3$ are done to address the dependence on the relative twist of the layers and are discussed in the Supplemental Material [23].)

Because graphene and CrI_3 are both layered van der Waals materials, the results presented below are only very weakly dependent on the horizontal registry between the two, as

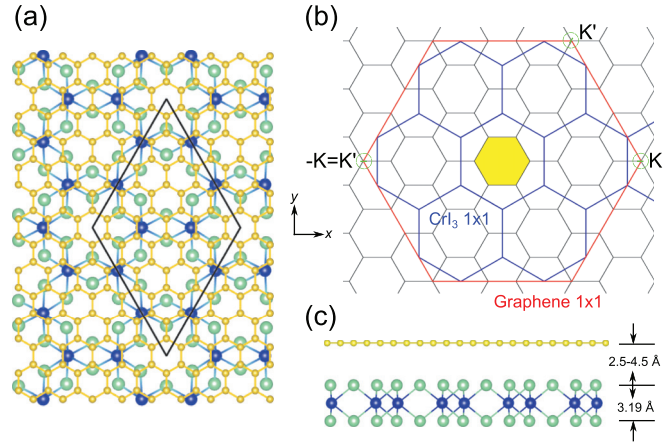

FIG. 1. (a) Top and (c) side views of the $(\sqrt{3} \times \sqrt{3})$ CrI_3–(5×5) graphene structure (C: yellow; Cr: blue; I: green), with the commensurate supercell given in black. (b) The Brillouin zones of the supercell (black; first Brillouin zone in yellow), (1×1) CrI_3 (blue), and (1×1) graphene (red). The green circles (and enclosed lines) denote the portion of k space where the graphene Dirac points occur.

verified by considering two different less symmetric registries. The supercell Brillouin zone, which is a factor of 25 (3) times smaller than that of graphene (CrI_3), is shown in Fig. 1(b). The interlayer separation is varied between 2.5 and 4.5 Å.

The calculations were performed using the Vienna Ab initio Simulation Package [30] within the generalized gradient approximation (GGA)+U rotationally invariant approximation [31], with the choice of $U = 1\,\text{eV}$, J=0. (As shown in Ref. [29], the CrI_3 gap decreases with increasing U, contrary to normal expectations. This choice of parameters provides a reasonable starting point for the CrI_3 electronic structure.) In addition, van der Waals DFT-D3 corrections [32] were included. The projector-augmented wave functions were expanded in plane waves up to 400 eV, the repeated slab geometry included a vacuum region of at least 20 Å, and a $27 \times 27 \times 1$ k-point mesh in the supercell was used for self-consistency, corresponding to a $135 \times 135 \times 1$ mesh for graphene; this mesh was sufficient for placing the Fermi level and for the optical conductivity calculations. Spin-orbit was included for some calculations (see Supplemental Material [23]) using the same parameters.

Each ferromagnetically coupled Cr has a magnetic moment of $3\,\mu_B$, and the moments are calculated (~0.4 meV/Cr) to be orientated perpendicular to the plane. The spin-polarized k-projected [33,34] bands of graphene around the K point and of CrI_3 at the calculated equilibrium graphene-CrI_3 separation of 3.75 Å are shown in Figs. 2(a) and 2(b), respectively. (The range of separations discussed here may be experimentally accessible: the calculated pressures are 1.4, 3.7, and 13.5 GPa for separations of 3.25, 3.0, and 2.5 Å, respectively.)

The top of the CrI_3 valence band and the lowest set of conduction bands are of majority spin (blue curves). The graphene Dirac point lies above the Fermi level in the conduction band of CrI_3, and opens up a gap in the CrI_3 bands along Γ-M [red circle in Fig. 2(b)]. The relative position of the graphene and CrI_3 bands varies with interlayer separation

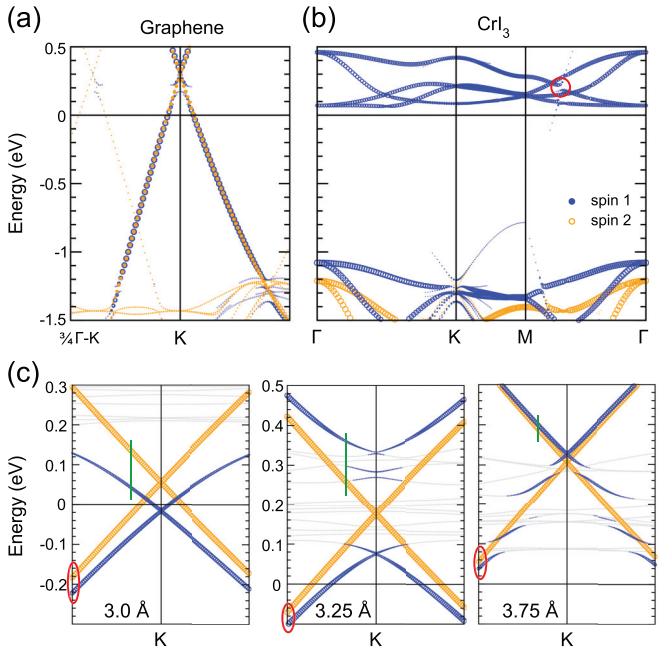

FIG. 2. k-projected bands of the graphene–CrI_3 magnetic system. Blue (orange) denote the majority (minority) spin of the CrI_3, and the size of the circles represents the relative weight. (a) Graphene k-projected bands around the K point ($\pm\frac{1}{4}$) along Γ-K of the (1×1) Brillouin zone, and (b) CrI_3 k-projected bands along the high symmetry directions of the (1×1) structure, both for a graphene–CrI_3 separation of 3.75 Å. (c) Close-ups of the graphene k-projected bands bands within $\pm\frac{1}{40}$ of K for different separations. The gray bands are ("folded" and CrI_3) bands with small weights. The green lines and red ovals show where the exchange splittings above and below the Dirac point, respectively, are measured.

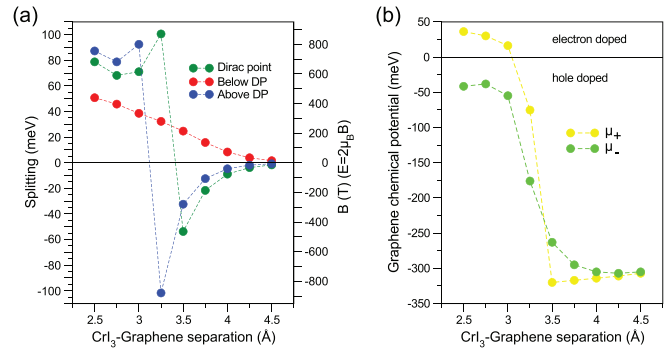

FIG. 3. (a) Exchange splittings (meV) and effective field (T), of the graphene states around K for different separations determined at the positions shown in Fig. 2(c) [above and below the Dirac point indicates the green line and red ovals, respectively, in Fig. 2(c)]. (b) The chemical potentials of graphene for each spin relative to the respective Dirac points.

(Fig. 2(c) and Supplemental Material Fig. S2 [23]): for separations of less than ∼3.2 Å, the graphene Dirac point is in the gap and then crosses into the CrI_3 conduction band. This behavior can be understood by noting that the calculated work functions and CrI_3 gap place the graphene Dirac point within the CrI_3 conduction band, for both the present GGA+U calculations and for hybrid Heyd–Scuseria–Ernzerhof functional calculations [14]. However, GW calculations for CrI_3 [29] increase the size of the gap, so that at the equilibrium separation the Dirac point may still be within the gap. Regardless, the present results can provide insight into the difference in expected behavior with the relative placement of the two sets of bands.

For all separations, Fig. 2(c), the minority ("spin 2") graphene bands maintain their linear dispersions, even including spin-orbit interaction (c.f., Figs. S3 and S4). The majority bands, on the other hand, interact and hybridize with the (majority spin) conduction band states even for smaller separations where the Dirac point is in the CrI_3 gap. Importantly, because of the proximity of the graphene to the ferromagnetic CrI_3, there are induced exchange splittings of the graphene bands. For larger separations, the majority graphene bands that overlap the GrI_3 conduction bands are strongly modified, whereas the minority bands retain the characteristic graphene dispersions.

The calculated splittings of the Dirac point and the bands above (below) measured at the indicated positions are given in Fig. 3(a). These splittings are large compared to the Zeeman splittings induced by an external field: the effective fields are in the range of 100 T. When the Dirac point is in the gap, the exchange splittings are normal in the sense that the majority states are deeper in energy than the minority. However, the exchange splitting of the Dirac point and the bands above reverse as the Fermi level of the combined system moves into the CrI_3 conduction band.

Because of the exchange splitting and the relative positions of the bands, the graphene is effectively doped, which can be described by spin-dependent chemical potentials, $\mu_\pm$, as shown in Fig. 3. For smaller separations with the Dirac points in the gap, $\mu_\pm$ are approximately equal and of opposite sign, i.e., no net doping. For larger separations, including the equilibrium one, the graphene becomes hole doped with $\mu_\pm \sim 0.3$ eV. The result is that for smaller separations when the Fermi level is in the gap, the position of the (minority) Dirac cone is closer to the Fermi level and determined by the size of the exchange splitting, while for larger separations doping determines the position; that the chemical potentials are approximately equal and much larger than the exchange splittings is physically related to the fact that local magnetic moments formation in graphene sheets is not favorable.

For graphene in external magnetic fields and nonzero chemical potential, the intraband contributions to σ_{xx} dominate over interband ones in the far-infrared optical conductivity, and the formation of Landau levels provide an explanation of the Hall conductivity σ_{xy}. Although the *effective* fields due to the proximity-induced exchange splittings are large, these do not create LLs; the formations of the minibands in the majority bands seen in Fig. 2(c) are due to interactions and hybridization with the CrI_3. The LLs formed in graphene in the presence of external magnetic fields or strain-induced pseudomagnetic fields [35] are both more localized in energy and have their broad momentum distribution peaked around K. Similar to LLs, however, these minibands change the dispersion and hence will modify the optical transitions.

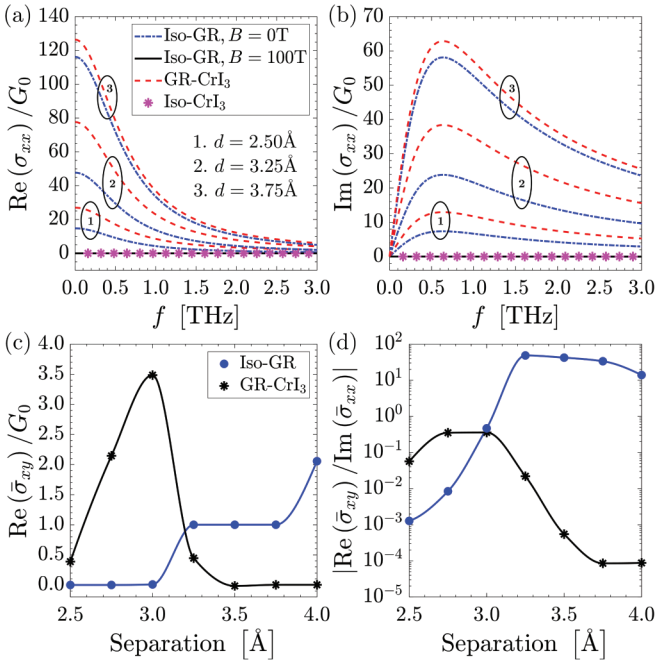

FIG. 4. (a), (b) Two-dimensional conductivity of graphene in the presence of the CrI_3 exchange field for separations $d \in \{2.5\,\text{Å}, 3.25\,\text{Å}, 3.75\,\text{Å}\}$. Also shown for comparison is the conductivity of isolated graphene (Iso-GR) computed assuming an external field of 100 T with chemical potential $\mu = -0.3$ eV [36], and the zero external field case using the spin dependent chemical potentials that correspond to each of the afformentioned separations (in both of the latter computations, $\Gamma = 2 \times 10^{12}$ s^{-1} and $T = 40$ K). (c) Off–diagonal element vs CrI_3-graphene separation compared with the isolated-graphene external bias case [where for each separation the value of effective field below the Dirac point from Fig. 3(a) was assumed. (d) The off-diagonal element normalized by the frequency average of the diagonal element. In (c), (d), the overbar indicates frequency average, as explained in the text. $G_0 = 2e^2/h$.

III. GRAPHENE CONDUCTIVITY AND SURFACE AND EDGE PLASMON POLARITONS DUE TO CrI_3 EXCHANGE FIELD

The computation of the intra- and interband contributions to graphene's conductivity in the presence of the CrI_3 exchange field is briefly described in the Supplemental Material [23]. Figure 4 shows the computed conductivity in the far-infrared and, for comparison, the conductivity computed (i) assuming isolated graphene in an external bias of 100 T and $\mu = -0.3$eV [36], the effective equilibrium exchange field and potential as described above; (ii) isolated graphene $B = 0$ T using $\mu^{\pm}$ plotted in Fig. 3(b) for separations $d \in \{2.5\,\text{Å}, 3.25\,\text{Å}, 3.75\,\text{Å}\}$; and (iii) the calculated CrI_3 conductivity [29], which is negligible at the considered frequencies. Figures 4(a) and 4(b) show the diagonal elements vs frequency, and Fig. 4(c) shows the off-diagonal element vs CrI_3-graphene separation (which are nondispersive in our calculation). For the external bias case, Fig. 4(c), the effective fields ("below the DP" values) for each "separation" from Fig. 3 were assumed. In Figs. 4(c) and 4(d), we show the mean conductivity for 0 to 5 THz. As an example, for the CrI_3-graphene data (for a separation of 3.75 Å), this mean is 33 G_0, and for isolated biased graphene ($B_0 = 100$ T), 0.03488 G_0.

The diagonal elements of the conductivity are dominated by the Drude intraband contribution at the considered frequencies ($\sigma_{xx}^{\text{2D-Drude}} = i\Omega/(\omega + 2i\Gamma)$, with the Drude weights Ω shown in Fig. S6), and resemble very closely the conductivity for isolated graphene with no magnetic bias, but with the exchange-field induced spin-dependent values of chemical potential $\mu^{\pm}$. Because of transfer of the Drude weight to the Landau levels in the case of an external bias, the exchange field diagonal conductivity is several orders of magnitude larger than the equivalent external field conductivity, i.e., for the external bias case, the formation of Landau levels depresses the diagonal conductivity away from the Landau level, while forcing the off-diagonal elements to be nonzero due to cyclotron motion of the charge carriers. This results in relatively large ratios of the off-diagonal to diagonal elements for the external bias, in contrast to the exchange bias case where the diagonal elements are relatively unaffected and hence the ratios are smaller.

For some separations (c.f., Fig. 3) the chemical potential is quite different for the two spins, as is the effective bias field. Therefore, for the external bias computation, we adjust the spins accordingly and sum over the two spins. For the off-diagonal elements, the exchange field values are similar in magnitude to the external bias case having the same effective field. Figure 4(d) shows the off-diagonal values of the conductivity normalized by the frequency average of the diagonal element since this ratio is an indication of the nonreciprocity of the material. Notably, the nonreciprocity of the exchange field case is much weaker than for the external field bias.

From Fig. 4, the CrI_3 conductivity is much smaller in magnitude than that of graphene. Since these effectively combine in parallel from an electromagnetic standpoint, we can ignore the presence of the CrI_3 in the electromagnetic calculations. This was confirmed by computing the dispersion of the CrI_3-graphene system including both conductivities, as in Ref. [37].

A. Bulk (Surface) SPPs

For the case of graphene having an arbitrary conductivity tensor and residing in a homogeneous medium characterized by μ_0 and ε, SPPs of an infinite 2D sheet satisfy a dispersion equation of the form $D(k_x, k_y) = 0$ [38], where

$$D(k_x, k_y) = k_x k_y(\sigma_{yx} + \sigma_{xy}) + \left(k_y^2 - k_1^2\right)\sigma_{yy} + \left(k_x^2 - k_1^2\right)\sigma_{xx} - 2ip\varepsilon\omega\left(1 + \tfrac{1}{4}\eta^2(\sigma_{xx}\sigma_{yy} - \sigma_{xy}\sigma_{yx})\right), \quad (1)$$

$p = \sqrt{k^2 - k_1^2}$, $k = |\mathbf{k}|$ is the in-plane wave number, and $k_1 = \omega\sqrt{\mu_0\varepsilon}$. The square root in p leads to a two-sheeted Riemann surface in the q plane, and associated branch cuts. The standard hyperbolic branch cuts [39] separate the proper (where $\mathrm{Re}(p) > 0$, such that the radiation condition as $|z| \to \infty$ is satisfied) and improper sheets.

In the presence of the exchange field, or an external magnetostatic bias, the conductivity tensor elements are

$$\sigma_{xx} = \sigma_{yy} = \sigma_d, \qquad \sigma_{xy} = -\sigma_{yx} = \sigma_o. \quad (2)$$

In this case, Eq. (1) reduces to

$$D(k) = \left(p^2 - k_1^2\right)s_d - ipk_1\left(1 + s_d^2 + s_o^2\right), \tag{3}$$

where $s_d = \eta\sigma_d/2$, $s_o = \eta\sigma_o/2$, and $\eta = \sqrt{\mu_0/\varepsilon}$, and $D(k) = 0$ can be solved to yield

$$k^{\pm} = k_1\left[\frac{1}{2^2 s_d^2}\left(-is^2 \pm \sqrt{4s_d^2 - s^4}\right)^2 + 1\right]^{1/2}, \tag{4}$$

where $s^2 = s_d^2 + s_o^2 + 1$. For $s_o = 0$, Eq. (4) becomes

$$k^{+} = k^{TM} = k_1\sqrt{1 - \frac{1}{s_d^2}}, \quad k^{-} = k^{TE} = k_1\sqrt{1 - s_d^2}, \tag{5}$$

for the transverse-magnetic (TM) and transverse-electric (TE) cases, respectively, where transverse is defined with respect to the radial coordinate. For isolated and unbiased graphene characterized by isotropic complex surface conductivity, $\sigma = \sigma' + i\sigma''$, a proper TE surface wave exists if and only if $\sigma'' < 0$, and a proper TM surface wave exists for $\sigma'' > 0$. If $\mu \neq 0$, pure TM and TE modes do not exist in the presence of a magnetic bias, although usually the modes retain similar characteristics (quasi-TM/TE).

B. Edge Surface Plasmon Polaritons

Assuming an out-of-plane magnetic bias and symmetry, bulk SPPs have reciprocal dispersion; breaking symmetry, for example, by introducing an interface, allows for plasmons with asymmetrical dispersion [40]. Specifically, here we introduce a graphene half-space, and consider the quasistatic modes that may propagate on the edge. This is a well-studied problem [41,42], and here we consider the exchange field case and, for comparison, the external bias case. Two different methods of analysis are presented in the Supplemental Material [23], and a new approximate solution for SPP edge dispersion is given there [Eq. (56)].

Figure 5 shows the bulk and edge dispersions for a graphene half-space due to the exchange fields corresponding to separations of 3.0 Å, Fig. 5(a), and 3.75 Å, Fig. 5(b). For 3-Å separation, the right-going edge mode exists until approximately 3 THz, above which the edge mode leaks into the bulk SPP (mathematically, it crosses onto an improper Riemann sheet through a branch point associated with the bulk mode wave number); the leaky mode (not shown) then approximately follows the bulk dispersion, with slightly lower wave number. In this case, the edge mode is strongly nonreciprocal (unidirectional). However, for the equilibrium separation of 3.75 Å separation, the edge mode is essentially reciprocal.

The bulk and edge dispersions for graphene in an external magnetic bias field are shown in Fig. 6. The edge modes flip directions upon reversing the bias field. Although the results were computed assuming $B = 100\,\mathrm{T}$, due to the normalization, the dispersion diagrams are essentially independent of B for $|B| \gtrapprox 1$ T. For the external bias case, the Landau levels are given by

$$M_n = \sqrt{2nv_F^2|eB|\hbar} \approx 36.3\ \mathrm{meV}\sqrt{n|B|}, \tag{6}$$

where $v_F \simeq 10^6$ m/s is the graphene electron Fermi velocity.

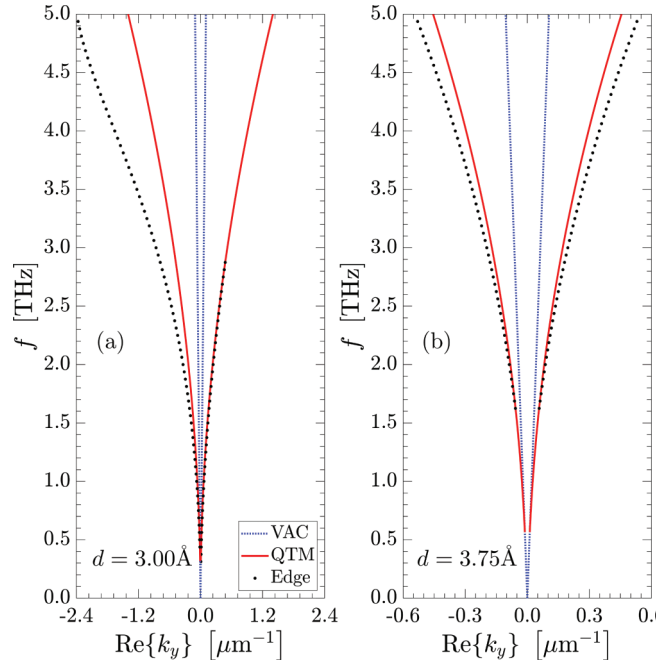

FIG. 5. Bulk (solid red) and edge (dots) TM-like dispersion of graphene modes in an exchange field for two CrI_3-graphene separations. VAC indicates vacuum dispersion.

For the exchange field (Fig. 5), the bulk SPPs are not gapped, whereas for the external bias case (Fig. 6) the bulk SPPs are strongly gapped. This is a result of the behavior of $\mathrm{Im}(\sigma)$: Since TM and quasi-TM modes require $\mathrm{Im}(\sigma) > 0$ for a proper surface wave, gaps appear for $\mathrm{Im}(\sigma) < 0$, which does not occur for the exchange case in the far-infrared, where the conductivity dispersion is Drude-like. In the external bias case, the formation of LLs causes this sign change at lower frequencies, resulting in the TM gap shown in Fig. 6.

Figures 7(a) and (7b) show edge SPP propagation length and guided wavelength on the graphene layer as a function of CrI_3-graphene separation. The SPP propagation length $1/2\,\mathrm{Im}(k_y)$ generally increases with separation, and decreases with increasing frequency. The SPP wavelength is quite long, $L_{\mathrm{SPP}}/\lambda_{\mathrm{SPP}} \ll 1$, and so the SPP seems not to be very useful.

The corresponding edge SPP propagation length and wavelength on the graphene layer in an external field as a function of the external bias are shown in Figs. 7(c) and 7(d). As the magnetic bias increases, the SPP propagation length increases, and $L_{\mathrm{SPP}}/\lambda_{\mathrm{SPP}} > 1$; for large magnetic bias, $L_{\mathrm{SPP}}/\lambda_{\mathrm{SPP}} \approx 6 - 8$. For $\mu = -0.3$ eV, the results are the same as shown in Fig. 7 for $B > 80$ T, since for larger chemical potentials the SPP is not well-formed and is not quasi-TM below a critical bias [43].

Figure 8 shows the edge SPP on the exchange-field biased graphene due to a dipole source in the vicinity of the graphene-vacuum edge, computed using COMSOL. In correspondence with the dispersion shown in Fig. 5, for the equilibrium separation of 3.75 Å the SPP is essentially reciprocal, as it is at 2.5 THz for separation 3 Å. However, for 3 Å and 4 THz, the SPP is unidirectional. However, because $L_{\mathrm{SPP}}/\lambda_{\mathrm{SPP}}$ is short, the SPP does not propagate well.

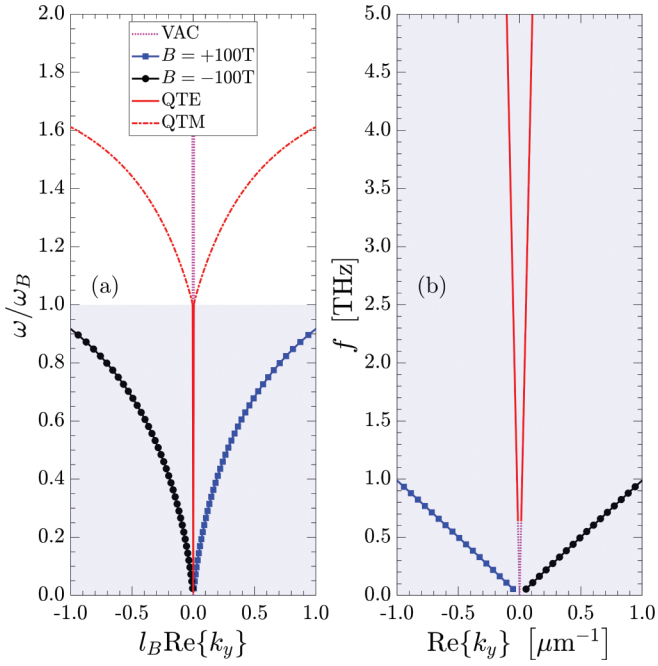

FIG. 6. Bulk (dashed red) and edge (dots) TM-like dispersion and bulk TE-like modes (solid red) for graphene in an external bias. The shaded region indicates the bulk band gap, $\omega_B = 526.2 \times 10^{12}$ is the frequency of the first Landau level, $\mu = -0.3$ eV, $T = 40$ K, $\Gamma = 2 \times 10^{12}$ s^{-1}, $B = 100$ T, and $l_B = \sqrt{\hbar/eB} = 2.6$ nm is the magnetic length.

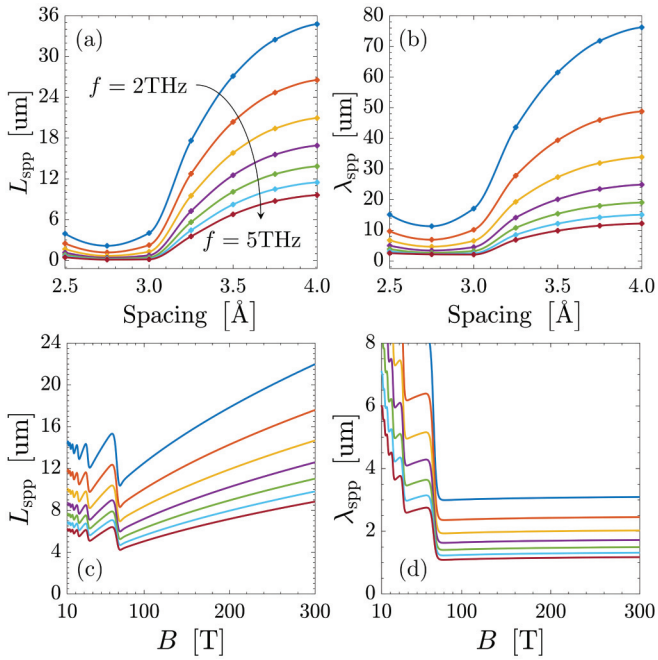

FIG. 7. (a) Edge SPP propagation length (left branch of Fig. 5) and (b) SPP wavelength on graphene in an exchange field as CrI_3-graphene separation varies. (c) Edge SPP propagation length and (d) SPP wavelength on graphene in an external bias for different frequencies. $\mu = 0.05$ eV, $T = 40$ K, $\Gamma = 2 \times 10^{12}$ s^{-1}. For (c) and (d), the first LL occurs at $8.8\sqrt{|B|}$, well beyond the considered frequencies. For comparison, from Fig. 3, for the separations 2.5, 3, 3.5, and 4 Å, the effective bias fields are 750, 600, 450, and 90 T, respectively.

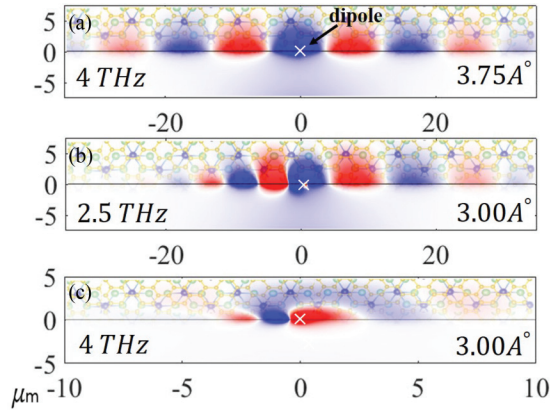

FIG. 8. Edge SPP launched by a dipole source near the graphene-vacuum edge for the exchange field magnetic bias corresponding to two CrI_3-graphene separations.

In contrast to Fig. 8, Fig. 9 shows the edge SPP on externally biased graphene due to a dipole source in the vicinity of the edge, computed using COMSOL. The size of the discontinuity is on the order of λ_{SPP} (e.g., the length of the discontinuity contour in the second panel is $5\lambda_{SPP}$). It is clear that as the magnetic bias increases, the SPP propagates further, in agreement with Fig. 7, while its wavelength increases. The edge SPP is clearly robust, and propagates around the discontinuity. Although there appears to be a weak field to the left of the source, it is due to the imperfect boundary condition at the edge of the computational domain. (Converting to the time domain shows that the field to the left of the source is actually traveling towards the right.)

IV. FARADAY ROTATION

Faraday rotation on magnetically biased graphene has been studied in [19,44], among other works. As discussed above,

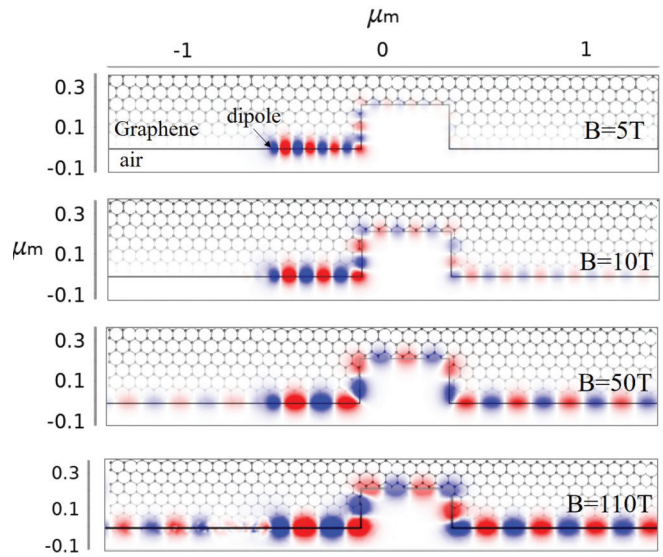

FIG. 9. Edge SPP launched by a dipole source near the graphene edge for several values of external magnetic bias. $f = 13.87$ THz, $\mu = 0.05$ eV, $T = 40$ K, $\Gamma = 2 \times 10^{12}$ s^{-1}.

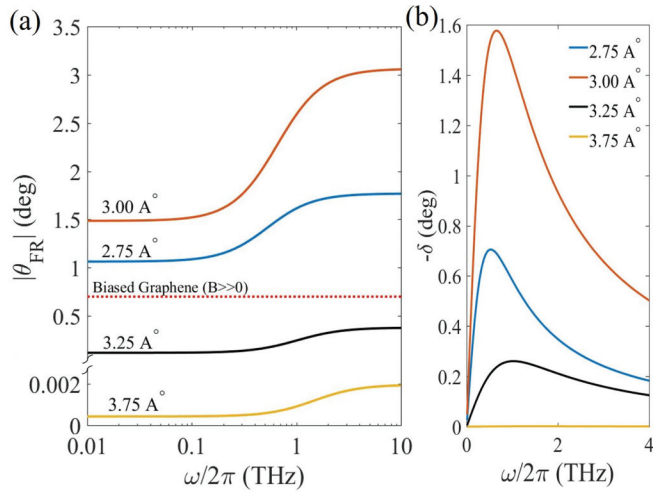

FIG. 10. (a) Faraday rotation and (b) ellipticity of the CrI_3-graphene heterostructure as a function of frequency for different separations. The dotted curve shows FR for externally-biased graphene using the effective field strengths from Fig. 3.

since the conductivity of the CrI_3 is much smaller than the conductivity of graphene at the considered frequencies, we can neglect the Faraday rotation contribution of the CrI_3, and only consider the FR of graphene under the influence of the exchange field. The Faraday rotation is computed as [45]

$$\theta_{\mathrm{FR}} = \frac{1}{2}\arg\left(\frac{t_{pp} - it_{ps}}{t_{pp} + it_{ps}}\right), \tag{7}$$

and the ellipticity as

$$\delta = \frac{|t_{pp} - it_{ps}|^2 - |t_{pp} + it_{ps}|^2}{|t_{pp} - it_{ps}|^2 + |t_{pp} + it_{ps}|^2}, \tag{8}$$

where $t_{pp} = E_p^t/E_p^i$, $t_{ps} = E_s^t/E_p^i$; $p = x, y$, $s = x, y$, $s \neq p$; and the superscripts indicate incident (i) or transmitted (t) fields. For graphene in a homogeneous medium, the transmission coefficients are

$$t_{xx} = \frac{4/\eta + 2\sigma_{xx}}{4\sigma_{xx} + \eta\left(\sigma_{xx}^2 + \sigma_{xy}^2\right) + 4/\eta}, \tag{9}$$

$$t_{xy} = \frac{2\sigma_{xy}}{4\sigma_{xx} + \eta\left(\sigma_{xx}^2 + \sigma_{xy}^2\right) + 4/\eta}, \tag{10}$$

where $\eta = \sqrt{\mu/\varepsilon}$.

Faraday rotations for the exchange field case are shown in Fig. 10 for various CrI_3-graphene separations. For closer-than-equilibrium separations, modest Faraday rotations are observed, but for the equilibrium separation, FR is negligible since σ_{xy}/σ_{xx} is small. In contrast, for externally biased graphene, Fig. 11, large Faraday rotations can be obtained. As B increases, the FR resonance first blueshifts [Fig. 11(a)], and eventually stabilizes in frequency [Fig. 11(b)] at the first LL, but the peak FR continues to increase with increasing B. Ellipticity behaves in a similar manner as FR.

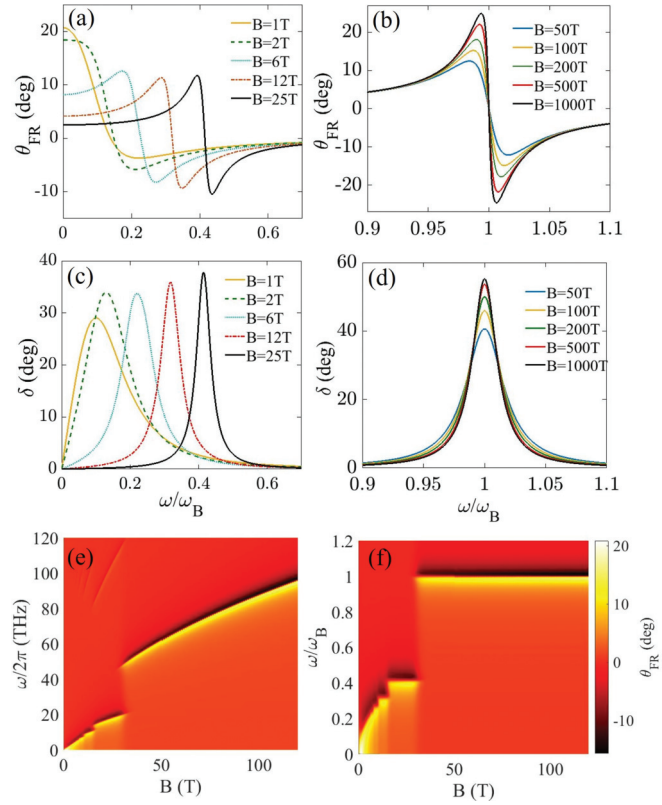

FIG. 11. (a),(b) Faraday rotation and (c),(d) ellipticity of graphene as a function of frequency for different external bias values, and (e),(f) density plots of Faraday rotation. ω_B is the frequency of the first Landau level for each bias. $\mu = 0.2\,\mathrm{eV}$, $T = 40\,\mathrm{K}$, and $\Gamma = 2\,\mathrm{THz}$.

V. CONCLUSIONS

We have examined exchange splitting in a monolayer chromium triiodide (CrI_3)–graphene vdW heterostructure using density-functional theory where effective exchange fields of hundreds of Tesla are predicted. These enormous fields serve as the magnetic bias for the graphene layer. Graphene conductivity and SPP properties for the exchange field were considered, and compared with the external bias case. Since no LLs occur for the exchange field, the resulting nonreciprocity is found to be considerably weaker than for an equivalent external field bias (where strongly nonreciprocal electromagnetic edge modes that are tightly confined, robust, and unidirectional are shown to exist). Faraday rotation due to the exchange field was also shown to be modest compared to the external bias case.

ACKNOWLEDGMENT

Funding for this research was provided by the National Science Foundation under Grant No. EFMA-1741673.

[1] K. S. Novoselov, A. K. Geim, S. V. Morozov, D. Jiang, Y. Zhang, S. V. Dubonos, I. V. Grigorieva, and A. A. Firsov, Electric field effect in atomically thin carbon films, Science. **306**, 666 (2004).

[2] S. D. Sarma, S. Adam, E. H. Hwang, and E. Rossi, Electronic transport in two-dimensional graphene, Rev. Mod. Phys. **83**, 407 (2011).

[3] M. A. McGuire, H. Dixit, V. R. Cooper, and B. C. Sales, Coupling of crystal structure and magnetism in the layered, ferromagnetic insulator CrI_3, Chem. Mater. **27**, 612 (2015).

[4] B. Huang, G. Clark, E. Navarro-Moratalla, D. R. Klein, R. Cheng, K. L. Seyler, D. Zhong, E. Schmidgall, M. A. McGuire, D. H. Cobden, W. Yao, D. Xiao, P. Jarillo-Herrero, and X. D. Xu, Layer-dependent ferromagnetism in a van der Waals crystal down to the monolayer limit, Nature (London) **546**, 270 (2017).

[5] J. Liu, Q. Sun, Y. Kawazoe, and P. Jena, Exfoliating biocompatible ferromagnetic Cr-trihalide monolayers, Phys. Chem. Chem. Phys. **18**, 8777 (2016).

[6] W.-B. Zhang, Q. Qu, P. Zhu, and C.-H. Lam, Robust intrinsic ferromagnetism and half semiconductivity in stable two-dimensional single-layer chromium trihalides, J. Mater. Chem. C **3**, 12457 (2015).

[7] B. Huang, G. Clark, D. R. Klein, D. MacNeill, E. Navarro-Moratalla, K. L. Seyler, N. Wilson, M. A. McGuire, D. H. Cobden, D. Xiao, W. Yao, P. Jarillo-Herrero, and X. Xu, Electrical control of 2D magnetism in bilayer CrI_3, Nat. Nanotech. **13**, 544 (2018).

[8] S. Jiang, L. Li, Z. Wang, K. F. Mak, and J. Shan, Controlling magnetism in 2D CrI_3 by electrostatic doping, Nat. Nanotech. **13**, 549 (2018).

[9] D. J. O'Hara, T. Zhu, A. H. Trout, A. S. Ahmed, Y. K. Luo, C. H. Lee, M. R. Brenner, S. Rajan, J. A. Gupta, D. W. McComb, and R. K. Kawakami, Room temperature intrinsic ferromagnetism in epitaxial manganese selenide films in the monolayer limit, Nano Lett. **18**, 3125 (2018).

[10] M. Kan, S. Adhikari, and Q. Sun, Ferromagnetism in MnX_2 (X = S, Se) monolayers, Phys. Chem. Chem. Phys. **16**, 4990 (2014).

[11] X. Li and J. Yang, $CrXTe_3$ (X = Si, Ge) nanosheets: two-dimensional intrinsic ferromagnetic semiconductors, J. Mater. Chem. C **2**, 7071 (2014).

[12] C. Gong, L. Li, Z. Li, H. Ji, A. Stern, Y. Xia, T. Cao, W. Bao, C. Wang, Y. Wang, Z. Q. Qiu, R. J. Cava, S. G. Louie, J. Xia, and X. Zhang, Discovery of intrinsic ferromagnetism in two-dimensional van der Waals crystals, Nature (London) **546**, 265 (2017).

[13] K. Zollner, P. E. Faria Junior, and J. Fabian, Proximity exchange effects in $MoSe_2$ and WSe_2 heterostructures with CrI_3: Twist angle, layer, and gate dependence, Phys. Rev. B **100**, 085128 (2019).

[14] J. Zhang, B. Zhao, T. Zhou, Y. Xue, C. Ma, and Z. Yang, Strong magnetization and Chern insulators in compressed graphene/CrI_3 van der Waals heterostructures, Phys. Rev. B **97**, 085401 (2018).

[15] N. Levy, S. A. Burke, K. L. Meaker, M. Panlasigui, A. Zettl, F. Guinea, A. H. Castro Neto, M. F. Crommie, Strain-induced pseudo–magnetic fields greater than 300 tesla in graphene nanobubbles, Science **329**, 544 (2010).

[16] J. Zhang, B. Zhao, Y. Yao, and Z. Yang, Robust quantum anomalous Hall effect in graphene-based van der Waals heterostructures, Phys. Rev. B **92**, 165418 (2015).

[17] P. Wei, S. Lee, F. Lemaitre, L. Pinel, D. Cutaia, W. Cha, F. Katmis, Y. Zhu, D. Heiman, J. Hone, J. S. Moodera, and C.-T. Chen, Strong interfacial exchange field in the graphene/EuS heterostructure, Nat. Mater. **15**, 711 (2016).

[18] Z. H. Qiao, S. A. Yang, W. X. Feng, W. K. Tse, J. Ding, Y. G. Yao, J. Wang, and Q. Niu, Quantum anomalous Hall effect in graphene from Rashba and exchange effects, Phys. Rev. B **82**, 161414(R) (2010).

[19] I. Fialkovsky and D. V. Vassilevich, Faraday rotation in graphene, Eur. Phys. J. B **85**, 384 (2012).

[20] T. M. Slipchenko, J. Schiefele, F. Guinea, and L. Martin-Moreno, Strain-induced large Faraday rotation in graphene at subtesla external magnetic fields, Phys. Rev. Research **1**, 033049 (2019).

[21] C. Cardoso, D. Soriano, N. A. García-Martínez, and J. Fernández-Rossier, Van der Waals Spin Valves, Phys. Rev. Lett. **121**, 067701 (2018).

[22] Y. V. Bludov, J. N. Gomes, G. A. Farias, J. Fernández-Rossier, M. I. Vasilevskiy, and N. M. R. Peres, Hybrid plasmon-magnon polaritons in graphene-antiferromagnet heterostructures, 2D Mater. **6**, 045003 (2019).

[23] See Supplemental Material at http://link.aps.org/supplemental/10.1103/PhysRevB.102.075435 for additional discussion of the DFT calculations and the derivation of the edge plasmon dispersion, which includes Refs. [24–28].

[24] M. Gajdoš, K. Hummer, G. Kresse, J. Furthmüller, and F. Bechstedt, Linear optical properties in the projector-augmented wave methodology, Phys. Rev. B **73**, 045112 (2006).

[25] A. L. Fetter, Edge magnetoplasmons in a bounded two-dimensional electron fluid, Phys. Rev. B **32**, 7676 (1985).

[26] W. Wang, J. Kinaret, and P. Apell, Excitation of edge magnetoplasmons in semi-infinite graphene sheets: Temperature effects, Phys. Rev. B **85**, 235444 (2012).

[27] G. W. Hanson and A. B. Yakovlev, *Operator Theory for Electromagnetics: An Introduction* (Springer, New York, 2002).

[28] X. Xia and J. J. Quinn, Multipole edge plasmons of two-dimensional electron-gas systems, Phys. Rev. B **50**, 8032 (1994).

[29] M. Wu, Z. Li, T. Cao, and Steven G. Louie, Physical origin of giant excitonic and magneto-optical responses in two-dimensional ferromagnetic insulators, Nat. Commun. **10**, 2371 (2019).

[30] G. Kresse and J. Furthmüller, Efficient iterative schemes for ab initio total-energy calculations using a plane-wave basis set, Phys. Rev. B **54**, 11169 (1996).

[31] S. L. Dudarev, G. A. Botton, S. Y. Savrasov, C. J. Humphreys, and A. P. Sutton, Electron-energy-loss spectra and the structural stability of nickel oxide: An LSDA+U study, Phys. Rev. B **57**, 1505 (1998).

[32] S. Grimme, J. Antony, S. Ehrlich, and S. Krieg, A consistent and accurate *ab initio* parametrization of density functional dispersion correction (DFT-D) for the 94 elements H-Pu, J. Chem. Phys. **132**, 154104 (2010); S. Grimme, S. Ehrlich, and L. Goerigk, J. Comput. Chem. **32**, 1456 (2011).

[33] J. W. Davenport, R. E. Watson, and M. Weinert, Linear augmented-Slater-type-orbital method for electronic-structure calculations. V. Spin-orbit splitting in Cu_3Au, Phys. Rev. B **37**, 9985 (1988); Y. Qi, S. H. Rhim, G. F. Sun, M. Weinert, and L. Li, Phys. Rev. Lett. **105**, 085502 (2010).

[34] M. X. Chen and M. Weinert, Layer k-projection and unfolding electronic bands at interfaces, Phys. Rev. B **98**, 245421 (2018).

[35] P. Nigge, A. C. Qu, É. Lantagne-Hurtubise, E. Mårsell, S. Link, G. Tom, M. Zonno, M. Michiardi, M. Schneider, S. Zhdanovich, G. Levy, U. Starke, C. Gutiérrez, D. Bonn, S. A. Burke, M. Franz, and A. Damascelli, Room temperature strain-induced Landau levels in graphene on a wafer-scale platform, Science Adv. **5**, eaaw5593 (2019).

[36] V. P. Gusynin, S. G. Sharapov, and J. P. Carbotte, Magneto-optical conductivity in graphene, J. Phys.: Condens. Matter **19**, 026222 (2007).

[37] G. W. Hanson, Quasi-TEM Modes Supported by a Graphene Parallel-Plate Waveguide, J. Appl. Phys. **104**, 084314 (2008).

[38] G. W. Hanson, Dyadic Green's Functions for an Anisotropic, Non-Local Model of Biased Graphene, IEEE Trans. Ant. Propagat. **56**, 747 (2008).

[39] A. Ishimaru, *Electromagnetic Wave Propagation, Radiation, and Scattering* (Prentice Hall, Upper Saddle River, NJ, 1991).

[40] R. Camley, Nonreciprocal surface waves, Surf. Sci. Rep. **7**, 103 (1987).

[41] D. B. Mast, A. J. Dahm, and A. L. Fetter, Observation of Bulk and Edge Magnetoplasmons in a Two-Dimensional Electron Fluid, Phys. Rev. Lett. **54**, 1706 (1985).

[42] Weihua Wang, Peter Apell, and Jari Kinaret, Edge plasmons in graphene nanostructures, Phys. Rev. B **84**, 085423 (2011).

[43] In the $B = 0$ case, the SPP is not formed for $\hbar\omega \gg \mu$ (states are not filled). In the external magnetic bias case, the value of B plays a role, with larger B moving the first LL to higher frequencies, increasing the band gap.

[44] I. Crassee, J. Levallois, A. L. Walter, M. Ostler, A. Bostwick, E. Rotenberg, T. Seyller, D. van der Marel, and A. B. Kuzmenko, Giant Faraday rotation in single- and multilayer graphene, Nat. Phys. **7**, 48 (2011).

[45] A. Ferreira, J. Viana-Gomes, Yu. V. Bludov, V. Pereira, N. M. R. Peres, and A. H. Castro Neto, Faraday effect in graphene enclosed in an optical cavity and the equation of motion method for the study of magneto-optical transport in solids, Phys. Rev. B **84**, 235410 (2011).

Supplemental Information for Exchange splitting and exchange-induced non-reciprocal photonic behavior of graphene in CrI_3-graphene vdW heterostructures

Alexander M. Holmes,[1,*] Samaneh Pakniyat,[1,†] S. Ali Hassani Gangaraj,[2,‡] Francesco Monticone,[2,§] George W. Hanson,[1,¶] and Michael Weinert[3,**]

[1] *Department of Electrical Engineering, University of Wisconsin-Milwaukee, 3200 N. Cramer St., Milwaukee, Wisconsin 53211, USA*

[2] *School of Electrical and Computer Engineering, Cornell University, Ithaca, NY 14853, USA*

[3] *Physics Department, University of Wisconsin-Milwaukee, Milwaukee, Wisconsin, 53211, USA*

(Dated: July 30, 2020)

I. GRAPHENE BANDS

A. Separation dependence

The spin-resolved DOS around the Fermi level of the combined system as a function of graphene-CrI_3 separation is shown in Fig. S1. The majority DOS has a large peak above the Fermi level arising from the CrI_3 conduction bands, as well as the graphene bands. For separations greater than ∼3.25 Å, the minority DOS show the characteristic V-shape due to the linear dispersion of the graphene bands around K, and similarly the majority DOS show the linear behavior in the gaps on either side of the CrI_3 peak. For closer approaches, however, the graphene contributions to the DOS of both spins are significantly distorted despite the fact that the Dirac point

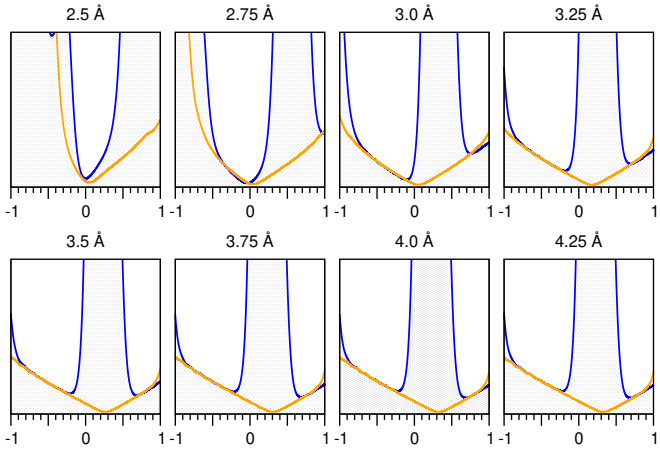

FIG. S1. Spin-resolved (majority: blue; minority: orange) density of states for the combined graphene-CrI_3 for different separations obtained by broadening each eigenvalue by the derivative of the Fermi function with k_BT=0.040 eV. The Fermi level is set to zero.

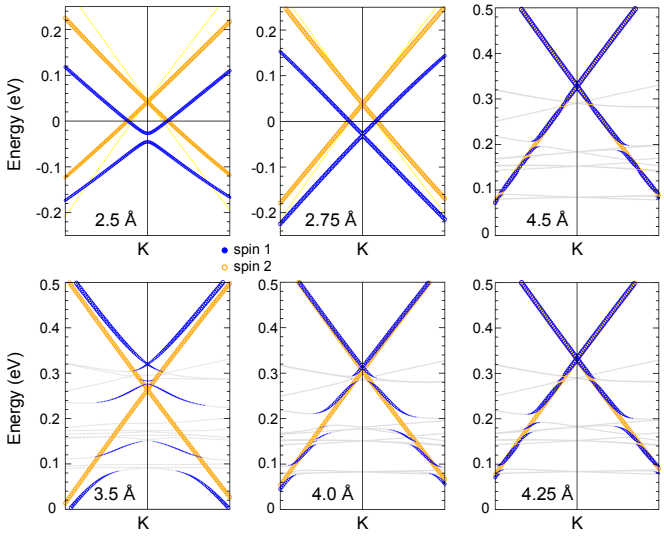

FIG. S2. k-projected bands of graphene around the K along ($\pm\frac{1}{40}$) Γ-K of the (1×1) Brillouin zone (c.f., Fig. 1 of the main text) for different graphene–CrI_3 separations. Blue (orange) denote the majority (minority) spin of the CrI_3, and the size of the circles represents the relative weight; gray symbols denote bands with small graphene weight. The yellow lines in the 2.5 and 2.75 Å plots are the isolated graphene bands shifted so the Dirac point coincides with that of the minority bands.

lies in the CrI_3 band gap.

The k-projected graphene bands for separations Δd in addition to Fig. 2(c) of the main text are shown in Fig. S2. For Δd=2.5 Å, the Fermi level is in the CrI_3 gap. The bands are strongly exchanged split and, in order to maintain charge neutrality, the majority states are electron-doped while the minority states are hole-doped. The majority – but not the minority – bands are strongly split, 18.5 meV, at the Dirac point due to interactions with the CrI_3 substrate. (The minority Dirac point has a small 0.3 meV gap.) This different behavior, which is noticeable at all separations, is a consequence of the fact that the nearby CrI_3 states are of majority character. In addition, although the dispersion of the minority bands is linear, the slope is noticeably smaller, with the difference decreasing as the separation increases.

As the graphene and CrI_3 move apart, the Fermi level moves into the CrI_3 (majority spin) conduction band.

* holmesam@uwm.edu
† pakniyat@uwm.edu
‡ ali.gangaraj@gmail.com
§ francesco.monticone@cornell.edu
¶ george@uwm.edu
** weinert@uwm.edu

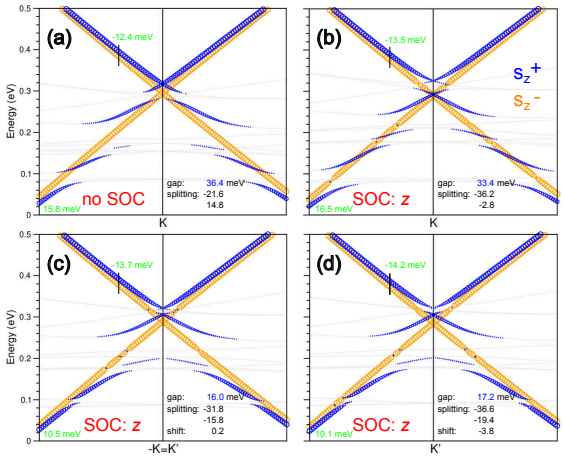

FIG. S3. k-projected bands of graphene around the various K points of the (1×1) Brillouin zone as in Fig. 1(b) of the main text ($\pm\frac{1}{40}$ along Γ-K) for the equilibrium separation of 3.75 Å: (a) No spin-orbit; and including spin-orbit with the Cr magnetic moments oriented along the z-axis: for (b) K, (c) −K=K', and (d) the K' rotated by 60^o. Blue (orange) symbols denote majority (minority) spins in (a) and projection along $\pm\hat{z}$ in (b)-(d), with the size corresponding to relative weight; gray symbols are for are states with small projected weights. The exchange splittings away from the Dirac points are given in green; for the Dirac points,"gap" refers to the splitting in the majority/s_z^+ bands, the two values of "splittings" are with respect to the Dirac point of the minority/s_z^- states, and "shift" in (c) and (d) is relative (b).

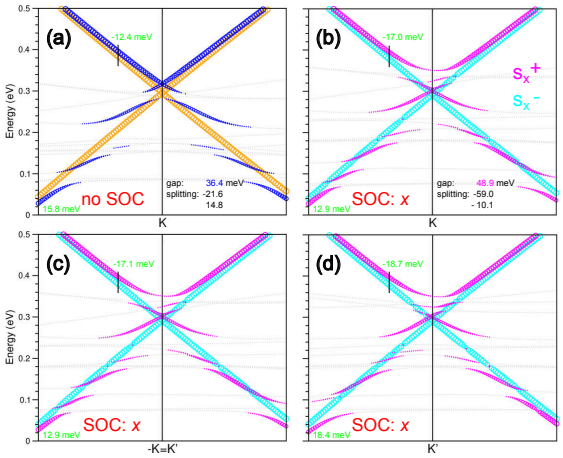

FIG. S4. As in Fig. S3 except the Cr moments are aligned along the x-axis.

As a consequence, the dispersions of the majority states below the Dirac point are modified via interactions and hybridization with the substrate bands, forming mini-bands in the graphene and CrI_3 bands. These mini-bands continue to exist even to quite large separations (e.g., 4.25 Å), and thus will affect the optical properties..

B. Spin-orbit effects

Without spin-orbit, the majority and minority bands separately are symmetric under the transformation $\vec{k} \to -\vec{k}$, i.e., the states at K and −K=K are degenerate. For a system with spin-orbit and magnetism (broken time-reversal symmetry), however, the these degeneracies no longer need to hold. In Fig. S3 the projected bands are shown for moments oriented along the z-axis, the calculated preferred direction. The bands at K, Fig. S3(b) differ from those at −K and K', Fig. S3(c,d), in the splittings and in the size and shape of the mini-bands. (There are also smaller differences between −K and K'.) These differences open the possibility of non-reciprocal valleytronic effects.

The direction of the magnetic moments causes noticeable effects on the dispersions. The results for moments oriented along the x-axis are shown in Fig. S4. As before, the graphene bands are essentially fully polarized along the axis of the Cr moments. The various splittings and the mini-bands change compared to those in for the moments along the z-axis.

C. Twist and Registry Dependence

The (5×5) graphene/($\sqrt{3}\times\sqrt{3}$) CrI_3 lattices have a relative orientation of 30°. Since twist angles of van der Waals materials are known to sometimes significantly affect the properties, we also considered a larger (2×2) CrI_3–($\sqrt{31}\times\sqrt{31}$) graphene supercell, Fig. S5(a), which

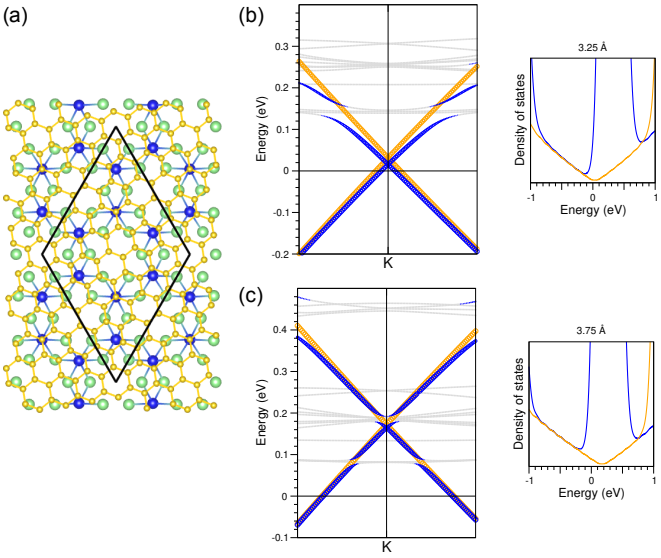

FIG. S5. (a) Top view of the (2×2) CrI_3–($\sqrt{31}\times\sqrt{31}$) graphene structure (C: yellow; Cr: blue; I: green), with the commensurate supercell given in black. k-projected graphene bands within $\pm\frac{1}{40}$ of the graphene K point and total density of states for (b) 3.25 Å and (c) 3.75 Å separation.

also has good lattice matching, albeit requiring slight changes in the relative lattice constants. The graphene lattice is twisted relative to the CrI_3 by ∼17.9°, or equivalently twisted by ∼12.1° compared to the other case. This twist will change where the graphene K point falls in the CrI_3 BZ, and thus which are the dominant CrI_3 states that the graphene Dirac states will interact with.

These calculations where limited to separations of 3.75 Å, which is near the equilibrium separation, and 3.25 Å, which is near where the Dirac point goes into the conduction band and the properties are rapidly changing. The calculations were done using the same parameters as the others, except a 21×21 k-point mesh was used.

The k-projected graphene bands around K are shown in Figs. S5(b,c). The overall density of states look similar to the previous cases, with the minority Dirac point near the band edge for 3.25 Å, and inside the conduction band for 3.75 Å. Because of the twist, the CrI_3 bands that coincide with the graphene K point have different dispersion, both being narrower and with different gaps between bands. The interaction with different CrI_3 states are responsible for the upturn in the minority DOS around +1 eV due to hybridization with higher lying minority CrI_3 bands.

For 3.25 Å, the Dirac points are below the conduction band edge in this part of reciprocal space, in contrast to the situation shown in Fig. 2. The exchange splitting of 17 meV of the Dirac point is smaller, but falls near the line in Fig. 3 since this is in the range where the exchange splitting is switching from positive to negative. Similar to the previous case, the majority band forms gaps and forms bind-bands with the interaction with the CrI_3 states. For the larger separation of 3.75 Å there are again formation of mini-bands, although the number are smaller because of the different number and grouping of bands in the relevant energy range.

That there are differences because of twist is not surprising since the energies and dispersions of the CrI_3 states (c.f., Fig. 2(b)) that will interact with the graphene Dirac states vary. Despite these changes, the qualitative behavior such as the formation of mini-bands remains, as do many of the other properties.

D. Optical Conductivity

The 2D optical conductivity for graphene-CrI_3 and isolated graphene were calculated within the independent particle approximation [1] and shown in Fig. S6. For graphene, with its linearly dispersing bands, the real part of the interband contribution of $\sigma^{xx}_{\rm 2D}(\omega)$ goes to $\frac{e^2}{4\hbar}$ for low frequencies; the calculated conductivity correctly obeys this limit, suggesting that the computational parameters (particularly k-point sampling) are adequate for the present purposes. For the composite system, the interband contribution

The intraband Drude-like contribution to the 2D conductivity tensor, $\sigma^{\rm Drude}_{\rm 2D}$, is given in terms of the plasma

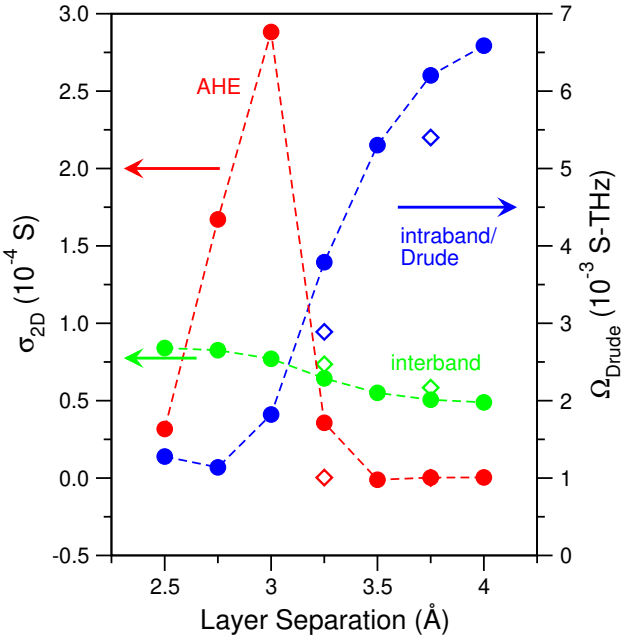

FIG. S6. Calculated 2D contributions to the optical properties: Drude intraband contribution, $\Omega_{\rm Drude}$ (blue); anomalous Hall, σ^{2D}_{xy} (red); and interband, σ^{2D}_{xx} (green). The open diamonds at 3.25 and 3.75 Å correspond to the twisted (2×2) CrI_3–$(\sqrt{31}\times\sqrt{31})$ graphene calculations.

frequency tensor ω_p^2

$$\left(\omega_p^2\right)_{\alpha\beta} \sim \sum_{n\boldsymbol{k}} f_{n\boldsymbol{k}} \frac{\partial^2 \epsilon_{n\boldsymbol{k}}}{\partial \boldsymbol{k}_\alpha \partial \boldsymbol{k}_\beta} \tag{1}$$

by

$$\sigma^{\rm Drude}_{\rm 2D} = \frac{L}{4\pi} \frac{(\hbar\omega_p)^2}{(\hbar\omega)^2 + (\hbar\gamma)^2} (\gamma + i\omega) \tag{2}$$

$$\equiv \Omega_{\rm Drude} \frac{\gamma_\nu + i\nu}{\nu^2 + \gamma_\nu^2}, \tag{3}$$

where $\omega = 2\pi\nu$ and $\gamma_\nu = 2\pi\gamma$. As expected, $\Omega_{\rm Drude}$ increases as the as the Fermi level crosses into the CrI_3 conduction band; the values for the twisted systems show similar behavior, although are calculated to be slightly smaller. (Only the xx component is appreciable.) For reasonable values of $\hbar\gamma$ of a few THz, the intraband dominates the interband contribution to σ_{xx}.

Because of the exchange field due to the CrI_3, there is a small contribution to σ_{xy}, but the largest contribution (within the present approximations) comes from the anomalous Hall effect (AHE),

$$\sigma^{\rm AHE}_{xy} \sim {\rm Im} \sum_{nm} (f_n - f_m) \langle u_m | \frac{d}{dk_x} u_n \rangle \langle u_m | \frac{d}{dk_y} u_n \rangle^* \ . \tag{4}$$

This term grows, and is large, as the graphene Dirac point and Fermi level approach the bottom of the CrI_3 conduction band, and then a sudden collapse as the Fermi level

crosses into the CrI_3. Thus, for the equilibrium spacing, this contribution is again small. If the large value of σ_{xy} is due to the proximity of the Fermi level near the bottom of the CrI_3 conduction band – and the existence of mini-bands in the graphene majority bands – it is possible that a GW or hybrid functional calculation that increases the gap might show a large AHE contribution at the equilibrium separation.

E. Graphene Conductivity in an External Bias

For the graphene conductivity in an external magnetic bias, we use the expressions in [2]. A prominent feature in strong external bias fields is the occurrence of Landau levels, whereas, as described in the main text, LLs are absent for the exchange field. It should be noted that in [2] spin splitting is ignored, so that summation over spin states just gives a multiplicative factor of 2. Here, spin splitting can be significant. At the equilibrium separation between graphene and CrI_3, the effective chemical potentials of the two spins are similar in magnitude, and have the same sign (main text, Fig. 3b). In this case, summing the conductivity in [2] over these two spins gives approximately the same result as the simple factor of 2. In the event of a strained system having smaller separation, the chemical potentials of the two spins can have opposite sign (main text, Fig. 3b). In that case, the two spin contributions can partially cancel, decreasing the magneto-optical conductivity terms.

II. EDGE MODE MODEL I: ELECTROSTATIC POTENTIAL

The following derivation loosely follows [3]. We also obtain a new approximate dispersion solution for the fundamental edge mode.

A. Electrostatic Green Function for a Homogeneous Single Interface Structure

Consider the dielectric interface structure in Fig. S7. For a charge distribution assumed to be in Region I ($z < 0$), Poisson's equation relates the electrostatic potential

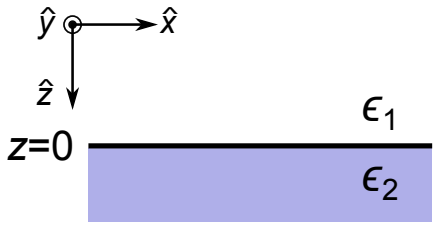

FIG. S7. Schematic of a two layer, laterally-infinite, dielectric medium.

to the net charge density as

$$\nabla^2 \left\{ \begin{array}{c} \Phi_1(\mathbf{r}) \\ \Phi_2(\mathbf{r}) \end{array} \right\} = \left\{ \begin{array}{c} -\rho(\mathbf{r})/\varepsilon_1 \\ 0 \end{array} \right\}, \tag{5}$$

subject to the boundary conditions at the interface

$$\Phi_1(\mathbf{r})|_{z=0} = \Phi_2(\mathbf{r})|_{z=0}, \tag{6}$$

$$\varepsilon_1 \frac{\partial}{\partial z}\Phi_1(\mathbf{r})\Big|_{z=0} = \varepsilon_2 \frac{\partial}{\partial z}\Phi_2(\mathbf{r})\Big|_{z=0}. \tag{7}$$

The associated Green function for each region then satisfies

$$\nabla^2 \left\{ \begin{array}{c} G_1(\mathbf{r},\mathbf{r}') \\ G_2(\mathbf{r},\mathbf{r}') \end{array} \right\} = \left\{ \begin{array}{c} -\delta(\mathbf{r}-\mathbf{r}')/\varepsilon_1 \\ 0 \end{array} \right\}, \tag{8}$$

subject to the same boundary conditions. The electrostatic potential in the ith region may then be written as

$$\Phi_i(\mathbf{r}) = \int G_i(\mathbf{r},\mathbf{r}')\,\rho(\mathbf{r}')\,d^3\mathbf{r}'. \tag{9}$$

In the spacial transform domain, it is easy to show that the particular solution of (8) in Region I is

$$G_1^p(\mathbf{k},\mathbf{r}') = G_1^p(\mathbf{k})\,e^{-i\mathbf{k}\cdot\mathbf{r}'}, \tag{10}$$

where $G_1^P(\mathbf{k}) = 1/\varepsilon_1|\mathbf{k}|^2$. The principal Green function in Region I, is then given by the inverse spacial transform of (10) with respect to z,

$$G_1^p(\mathbf{q},z,z') = \frac{1}{2\pi}\int_{-\infty}^{\infty} dk_z G^p(\mathbf{k})\,e^{ik_z(z-z')} \tag{11}$$

$$= \frac{1}{2\varepsilon_1 q}e^{-q|z-z'|}, \tag{12}$$

where $\mathbf{q} \equiv \hat{\mathbf{x}}k_x + \hat{\mathbf{y}}k_y$ and $q \equiv ||\mathbf{q}|| = \sqrt{k_x^2+k_y^2}$. In addition to the principal Green function in Region I, we add a homogeneous contribution $G_1^H(\mathbf{q},z)$ satisfying $\nabla^2 G_1^H = 0$. Since there is no source terms in Region II, the Green function there consists only of a homogeneous term, $G_1(\mathbf{q},z,z') = G_2^H(\mathbf{q},z)$ where $G_2^H(\mathbf{q},z)$ satisfies $\nabla^2 G_2^H = 0$. It is easy to show that

$$G_1^H = A(\mathbf{q})\,e^{qz}, \tag{13}$$

$$G_2^H = B(\mathbf{q})\,e^{-qz}, \tag{14}$$

where $A(\mathbf{q})$ and $B(\mathbf{q})$ are determined by applying the boundary conditions (6)-(7) at the interface. For $z' \le 0$, it follows that

$$G_1(\mathbf{q},z,z') = G_1^p(\mathbf{q},z,z') + A(\mathbf{q})\,e^{qz}, \tag{15}$$

$$G_2(\mathbf{q},z,z') = B(\mathbf{q})\,e^{-qz}, \tag{16}$$

where

$$A(\mathbf{q}) = \frac{1}{2\varepsilon_1}\frac{\varepsilon_1-\varepsilon_2}{\varepsilon_1+\varepsilon_2}\frac{e^{qz'}}{q}, \tag{17}$$

$$B(\mathbf{q}) = \frac{1}{\varepsilon_1+\varepsilon_2}\frac{e^{qz'}}{q}. \tag{18}$$

In the limit $z' \to 0$, we obtain the Green function for a source positioned at the interface,

$$G(\mathbf{q}, z, 0) = \frac{1}{2\bar{\varepsilon}} \frac{e^{-q|z|}}{q}, \tag{19}$$

where $\bar{\varepsilon} \equiv (\varepsilon_1 + \varepsilon_2)/2$. This Green function accounts for the background structure that will host the graphene.

B. Charge Density on Semi-Infinite Graphene

In this section, we consider a 2D charge density on graphene localized at $z = 0$. The graphene exists for $x < 0$, invariant with respect to y. The charge density is given by

$$\rho(\mathbf{r}) = \rho_s(x)\,\delta(z)\,e^{ik_y y}, \tag{20}$$

where $\rho_s(x)$ denotes the surface charge density at the interface. Because the electrostatic potential is also invariant with respect to y, we write $\Phi(\mathbf{r}) = \Phi(x, z)\,e^{ik_y y}$. Application of (9) leads to

$$\Phi(x, z) = \int_{-\infty}^{\infty} dx' G(x, x', z, 0)\,\rho_s(x'), \tag{21}$$

where

$$G(x, x', z, 0) = \frac{1}{2\bar{\varepsilon}} \int_{-\infty}^{\infty} \frac{dk_x}{2\pi} \frac{e^{-q|z|}}{q} e^{ik_x(x-x')} \tag{22}$$

$$= \frac{1}{2\pi\bar{\varepsilon}} K_0\left(|k_y| \sqrt{(x-x')^2 + z^2}\right), \tag{23}$$

with K_0 denoting the zero-order modified Bessel function of the second kind. The absolute value $|k_y|$ arises from having $q = \sqrt{k_x^2 + k_y^2}$.

The continuity equation relates the surface charge density to the surface current at the interface by $i\omega\rho_s(x) = \nabla \cdot \mathbf{J}_s(x)$ where $\mathbf{J}_s(x) = \Theta(-x)\,\bar{\sigma} \cdot -\nabla\Phi(x, z)|_{z=0}$. The components of the current expand to

$$J_{sx}(x) = -\Theta(-x)\left[ik_y\sigma_{xy} + \sigma_{xx}\frac{d}{dx}\right]\Phi(x, 0), \tag{24}$$

$$J_{sy}(x) = -\Theta(-x)\left[ik_y\sigma_{yy} + \sigma_{yx}\frac{d}{dx}\right]\Phi(x, 0), \tag{25}$$

which are used in the continuity equation to obtain $\rho_s(x) \equiv \delta(-x)\,\rho_e(x) + \Theta(-x)\,\rho_b(x)$, where

$$\rho_e(x) \equiv \hat{D}_e(x)\,\Phi(x, 0), \tag{26}$$

$$\rho_b(x) \equiv \hat{D}_b(x)\,\Phi(x, 0), \tag{27}$$

such that

$$\hat{D}_e(x) \equiv k_y\chi_{xy} + \eta_{xx}\frac{d}{dx}, \tag{28}$$

$$\hat{D}_b(x) \equiv k_y^2\eta_{yy} - k_y(\chi_{xy} + \chi_{yx})\frac{d}{dx} - \eta_{xx}\frac{d^2}{dx^2}, \tag{29}$$

where we define $\eta_{\alpha\alpha} \equiv \sigma_{\alpha\alpha}/i\omega$ and $\chi_{\alpha\beta} \equiv \sigma_{\alpha\beta}/\omega$ for $\alpha, \beta \in \{x, y\}$. Substituting (26)-(27) into (9), we have

$$\Phi(x, z) = \int_{-\infty}^{\infty} G(x, x', z, 0)\,\rho_s(x') \tag{30}$$

$$= G(x, 0, z, 0)\,\rho_e(0) + \int_{-\infty}^{0} dx' G(x, x', z, 0)\,\rho_b(x'), \tag{31}$$

where $\rho_e(0)$ and $\rho_b(x)$ should be interpreted as the charge density at the edge ($x = 0$) and in the bulk region ($x < 0$), respectively. Setting $z = 0$, we obtain an integro-differential equation for the potential in the plane of the interface,

$$\phi(x) = g(x, 0)\,\rho_e(0) + \int_{-\infty}^{0} dx' g(x, x')\,\rho_b(x'), \tag{32}$$

where $\phi(x) \equiv \Phi(x, 0)$ and $g(x, x') \equiv G(x, x', 0, 0)$.

We now expand the potential in terms of Laguerre polynomials,

$$\phi(x) = e^{|k_y|x} \sum_{n=0}^{\infty} c_n L_n(-2|k_y|x), \tag{33}$$

for which we have the orthogonality condition

$$\int_{-\infty}^{0} e^{2|k_y|x} L_m(-2|k_y|x)\,L_n(-2|k_y|x)\,dx = \frac{\delta_{nm}}{2|k_y|}. \tag{34}$$

Exploiting orthogonality by multiplying both sides sides of (32) by $e^{|k_y|x}L_m(-2|k_y|x)$ and integrating over x from 0 to ∞ leads to the dispersion relation

$$\frac{c_m}{2|k_y|} = \sum_{n=0}^{\infty} c_n A_{mn}, \tag{35}$$

where

$$A_{mn} \equiv J_{mn} + \eta_{xx}(2n+1)\,I_m + \mathrm{sgn}(q_y)\,\chi_{xy} I_m, \tag{36}$$

with

$$I_m \equiv |k_y| \int_{-\infty}^{0} dx e^{|k_y|x} L_m(-2|k_y|x)\,g(x, 0), \tag{37}$$

$$J_{mn} \equiv \int_{-\infty}^{0}\int_{-\infty}^{0} dx dx' G(x, x')\,\hat{D}_b(x')\,e^{|k_y|(x+x')} \times L_m(-2|k_y|x)\,L_n(-2|k_y|x'). \tag{38}$$

Making the change of variable $y \equiv |k_y|\,x$, reduces (37)-(38) to

$$I_m = \int_{-\infty}^{0} dy G(y, 0)\,e^y L_m(-2y), \tag{39}$$

$$J_{mn} = \int_{-\infty}^{0}\int_{-\infty}^{0} dy dy' G(y, y')\,\hat{D}_b(y')\,e^{(y+y')} \times L_m(-2y)\,L_n(-2y'). \tag{40}$$

where

$$G\left(y,y'\right)=\frac{1}{2\pi\bar{\varepsilon}}K_0\left(\left|y-y'\right|\right), \tag{41}$$

$$\hat{D}_b\left(y'\right)=\eta_{yy}-\mathrm{sgn}\left(q_y\right)\left(\chi_{xy}+\chi_{yx}\right)\frac{d}{dy}-\eta_{xx}\frac{d^2}{dy^2}\ . \tag{42}$$

Note that in this work, we assume $\sigma_{xx}=\sigma_{yy}$ and $\sigma_{xy}=-\sigma_{yx}$, which significantly reduces (40) to

$$J_{mn}=-\eta_{xx}\hat{S}\left(y,y'\right)G\left(y,y'\right)e^{\left(y+y'\right)} \times L_m\left(-2y\right)\frac{d^2}{dy'^2}L_{n+1}\left(-2y'\right), \tag{43}$$

which is straight forward to derive obtain using the recursive formulas

$$e^{-y'}\frac{d}{dy'}e^{y'}L_n\left(-2y'\right)=\frac{d}{dy'}L_{n+1}\left(-2y'\right)-L_n\left(-2y'\right), \tag{44}$$

$$e^{-y'}\frac{d^2}{dy'^2}e^{y'}L_n\left(-2y'\right)=\frac{d^2}{dy'^2}L_{n+1}\left(-2y'\right)+L_n\left(-2y'\right). \tag{45}$$

Truncating the expansion to $N+1$ terms allows us to cast (35) as a standard eigenvalue equation

$$\begin{bmatrix} A_{00} & A_{01} & \cdots & A_{0N} \\ A_{10} & A_{11} & \cdots & A_{1N} \\ \vdots & \vdots & \ddots & \vdots \\ A_{N0} & A_{N1} & \cdots & A_{NN} \end{bmatrix}\begin{bmatrix} c_0 \\ c_1 \\ \vdots \\ c_N \end{bmatrix}=\lambda\begin{bmatrix} c_0 \\ c_1 \\ \vdots \\ c_N \end{bmatrix}, \tag{46}$$

where $\lambda\equiv 1/2\left|k_y\right|$.

C. Surface Charge Density

Once the eigenvalue equation is solved for $\{c_n\}$, one can obtain numerical solutions for the potential and the surface charge density. Using (26), (27), and (33), it can be shown that

$$\rho_e\left(y\right)=\left|k_y\right|e^y\sum_{n=0}^{\infty}c_n\left[\left(\mathrm{sgn}\left(k_y\right)\chi_{xy}-\eta_{xx}\right)L_n\left(-2y\right)+\eta_{xx}\frac{d}{dy}L_{n+1}\left(-2y\right)\right] \tag{47}$$

$$\rho_b\left(y\right)=k_y^2e^y\sum_{n=0}^{\infty}c_n\left[\left(\eta_{yy}-\eta_{xx}+\mathrm{sgn}\left(q_y\right)\left(\chi_{xy}+\chi_{yx}\right)\right)\times L_n\left(-2y\right)-\mathrm{sgn}\left(q_y\right)\left(\chi_{xy}+\chi_{yx}\right)\frac{d}{dy}L_{n+1}\left(-2y\right)-\eta_{xx}\frac{d^2}{dy^2}L_{n+1}\left(-2y\right)\right] \tag{48}$$

Then, using $L_n\left(0\right)=1$ and $L_n'\left(0\right)=-n$, we obtain

$$\rho_e\left(0\right)\equiv\left|k_y\right|\sum_{n=0}^{\infty}c_n\left[\mathrm{sgn}\left(k_y\right)\chi_{xy}+\left(2n+1\right)\eta_{xx}\right]\ . \tag{49}$$

Assuming $\sigma_{xx}=\sigma_{yy}$ and $\sigma_{xy}=-\sigma_{yx}$,

$$\rho_b\left(y\right)=-\eta_{xx}k_y^2e^y\sum_{n=0}^{\infty}c_n\frac{d^2}{dy^2}L_{n+1}\left(-2y\right) \tag{50}$$

Figure S8 shows bulk and edge charge density at several values of external magnetic bias.

D. Approximating the Dispersion Relation

To a good approximation, the edge dispersion within the first TM band gap is obtained by considering only the $n=0$ term in the expansion (33). With the assumption that $\sigma_{xx}=\sigma_{yy}$ and $\sigma_{xy}=-\sigma_{yx}$, we find $J_{00}=0$, leading to

$$\left|k_y\right|=\left[2I_0\left(\eta_{xx}\pm\chi_{xy}\right)\right]^{-1}, \tag{51}$$

where

$$I_0=\left|k_y\right|\int_{-\infty}^{0}dxe^{\left|k_y\right|x}g\left(x,0\right), \tag{52}$$

such that

$$g\left(x,0\right)=\frac{1}{2\bar{\varepsilon}}\int_{-\infty}^{\infty}\frac{dk_x}{2\pi}\frac{1}{q}e^{ik_xx}, \tag{53}$$

which we approximate by expanding $q=\sqrt{k_x^2+k_y^2}$ about $k_x=0$,

$$\sqrt{k_x^2+k_y^2}\simeq\left|k_y\right|+\frac{k_x^2}{2\left|k_y\right|}\ . \tag{54}$$

This leads to the closed form approximate solution of (53)

$$g\left(x,0\right)\simeq g_0\left(x,0\right)\equiv\frac{1}{2\bar{\varepsilon}\sqrt{2}}e^{-\sqrt{2}\left|k_y\right|\left|x\right|}, \tag{55}$$

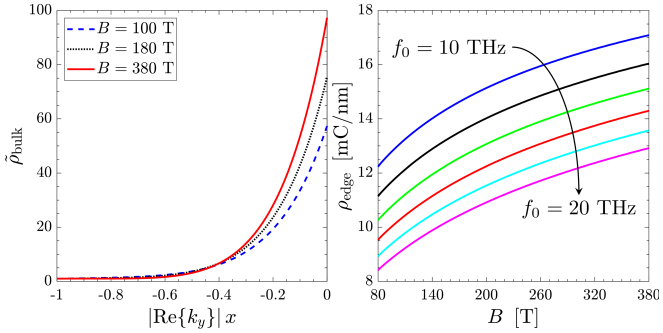

FIG. S8. (a) Bulk and (b) edge charge density for graphene in an external magnetic field. $\tilde{\rho}_{\mathrm{bulk}}$ is the bulk charge density normalized by ρ_{bulk} at $k_xx=-1$, and $\tilde{\rho}_{\mathrm{edge}}$ is the edge charge density normalized by ρ_{edge} at $B=10$T. $\mu=-0.3$eV, $T=40$K, and $\Gamma=2\times10^{12}$/s.

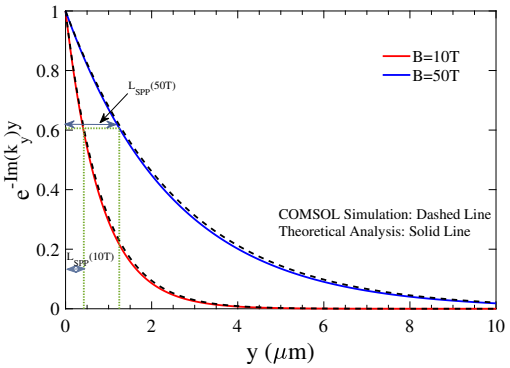

FIG. S9. Decay of edge plasmon, comparing perturbative solution for introducing loss (using (46)), and full solution of Maxwell's equations (COMSOL) for graphene in an external magnetic field. Frequency is 14 THz and $\mu = 0.05$ eV, $T = 40$K, $\Gamma = 2 \times 10^{12}$ rad/s.

which we use in (58), simplifying the dispersion relation to

$$|k_y| = \bar{\varepsilon} \frac{1+\sqrt{2}}{\eta_{xx} \pm \chi_{xy}} \ . \tag{56}$$

We find this result better approximates the exact edge mode dispersion than that used in previous works [4], [5],

$$|k_y| = \bar{\varepsilon} \frac{3\eta_{xx} - \mathrm{sgn}\,(k_y)\, 2\sqrt{2}\chi_{xy}}{\eta_{xx}^2 - \chi_{xy}^2} \ . \tag{57}$$

E. Material Loss

In statics, there is no concept of loss. However, our interest is in the quasi-static regime, such that we can perturb the system slightly by introducing a non-zero scattering rate Γ in the conductivity. Then, we can make the replacement

$$|k_y| \to k_y = \begin{cases} +\mathrm{Re}\,(k_y) + i\mathrm{Im}\,(k_y) & \mathrm{Re}\,(k_y), \mathrm{Im}\,(k_y) > 0 \\ -\mathrm{Re}\,(k_y) - i\mathrm{Im}\,(k_y) & \mathrm{Re}\,(k_y), \mathrm{Im}\,(k_y) < 0 \end{cases} \tag{58}$$

which ensures that the wave decays in the case of both forward and backward propagation. This results in complex-valued wavenumbers for the edge dispersion from both the exact method (46) and from the approximate value (56). As a check, we compared decay rates of the edge SPP generated using this perturbative approach and the result found via COMSOL. Figure S9 shows good agreement between the two methods for graphene in an external magnetic field.

Figure S10 shows the bulk and edge dispersion for graphene in an external magnetic bias field. The edge modes were computed using the exact quasi-static analysis (Eq. (46)), and a comparison between the exact and approximate edge dispersion solutions is also shown. Although the results were computed assuming $B = 100$T, due to the normalization the dispersion diagrams are essentially independent of B for $|B| \gtrapprox 1$ T.

III. EDGE MODE MODEL: CHARGE DENSITY APPROACH

The edge dispersion can be determined via an alternative method using the charge density.

A. 2D Bulk Mode

The quasi-static edge mode is obtained using an expansion of the charge density, rather than the potential, in Laguerre polynomials. Starting with a 2D conductivity tensor

$$\boldsymbol{\sigma} = \begin{bmatrix} \sigma_{xx} & \sigma_{xy} \\ \sigma_{yx} & \sigma_{yy} \end{bmatrix} \tag{59}$$

with $\sigma_{xx} = \sigma_{yy}$ and $\sigma_{yx} = -\sigma_{xy}$, it is assumed that the total electron density can be represented by $n_0 + n$, where n_0 is the ground state electron density and n is the corresponding fluctuation ($|n| \ll |n_0|$). The electron fluid is confined to the $z = 0$ plane. From charge conservation, $\nabla \cdot \boldsymbol{j} = -ie\omega n$, and $\boldsymbol{j} = \boldsymbol{\sigma} \cdot \boldsymbol{E}$,

$$n = \frac{1}{-ie\omega} \left[\sigma_{xx} \left(-\frac{\partial^2}{\partial y^2} - \frac{\partial^2}{\partial x^2} \right) \phi - \frac{\partial \sigma_{xx}}{\partial x} \frac{\partial \phi}{\partial x} - \frac{\partial \sigma_{xy}}{\partial x} \frac{\partial \phi}{\partial y} \right] \tag{60}$$

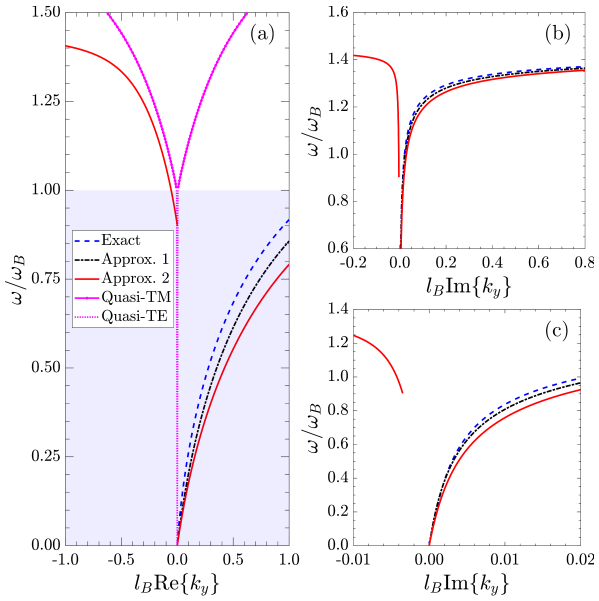

FIG. S10. Bulk (pink) and edge dispersion of graphene modes for real-part (a) and imaginary part (b)-(c) of wavenumber for graphene in an external magnetic field. The shaded region indicates the bulk band gap, and ω_B is the frequency of the first Landau level. Approx. 1 is using (56) and Approx. 2 is using (57); $\mu = -0.3$eV, $T = 40$K, $\Gamma = 2 \times 10^{12}$/s, $B = 100$T. $l_B = \sqrt{\hbar/eB}$ is the magnetic length.

where ϕ is the electrostatic potential, related to the electric field by $\boldsymbol{E} = -\nabla\phi$.

We first solve for the bulk modes of a laterally-infinite 2D electron fluid. In this case, Poisson's equation is

$$\nabla^2\phi = \frac{ne}{\epsilon_0}\delta(z). \tag{61}$$

We assume plane wave solutions proportional to $e^{i(\boldsymbol{q}\cdot\boldsymbol{r}-\omega t)}$, where $\boldsymbol{q}$ is the in-plane wavevector, and where the potential amplitude $\phi(z)$ depends on the distance from the plane as well as on the in-plane wavevector. It is straightforward to show that the solution has the form

$$\phi_q(z) = -\frac{n_q e}{2\epsilon_0 q}e^{-q|z|}, \tag{62}$$

where n_q is the corresponding amplitude for the electron density fluctuation. Note that in the quasi-static case the in-plane wavenumber q also serves to govern vertical decay. Assuming no disruption in the conductivity in the $x-y$ plane, $\partial\sigma_{ij}/\partial x = 0$, and Eq. (60) can be simplified as $n = (\sigma_{xx}/ie\omega)\nabla^2\phi$. Replacing ϕ by Eq. (62) yields the equation for the 2D quasi-static bulk SPP modes,

$$\omega\epsilon_0 + \frac{iq\sigma_{xx}}{2} = 0. \tag{63}$$

B. 2D Edge Mode

Here we suppose the 2D electron fluid is confined to $z = 0$ and occupies the half-plane on the negative side of the x-axis. From Eq. (60) we obtain

$$\begin{aligned} ie\omega n &= \sigma_{xx}\nabla^2\phi - \sigma_{xx}\delta(x)\frac{\partial\phi}{\partial x} - \sigma_{xy}\delta(x)\frac{\partial\phi}{\partial y} \\ &= \sigma_{xx}\nabla^2\phi + j_x\delta(x), \end{aligned} \tag{64}$$

where from $\boldsymbol{j} = \boldsymbol{\sigma}\cdot\boldsymbol{E}$ we obtain $j_x = -\sigma_{xx}\partial_x\phi - \sigma_{xy}\partial_y\phi$; the delta functions arise from derivatives of $\sigma_{i,j} = \sigma_{i,j}U(-x)$, where $U(x)$ is the unit step function. The above equation represents a singularity for the current along the x-axis at the edge, suggesting nonzero charge accumulation at the edge, $n = n_b(x) + n_e\delta(x)$ where $n_b(x)$ is the fluctuation in the bulk and n_e represents the accumulation at $x = 0$. Replacing n by $n_b(x) + n_e\delta(x)$ in the above equation,

$$ie\omega(n_b + n_e\delta(x)) = \sigma_{xx}\nabla^2\phi - \sigma_{xx}\delta(x)\frac{\partial\phi}{\partial_x} - \sigma_{xy}\delta(x)\frac{\partial\phi}{\partial y}.$$

Equating the non-singular terms on the left and right hand sides of the above equation leads to

$$\left(\frac{\partial^2}{\partial x^2} - q^2\right)\phi = \frac{ie\omega}{\sigma_{xx}}n_b(x), \tag{65}$$

where $q = q_y$ here and below. Equating the singular terms leads to

$$\left[\left(\frac{\partial}{\partial x} + iq\frac{\sigma_{xy}}{\sigma_{xx}}\right)\phi\right]_{x=0^-} = -\frac{ie\omega}{\sigma_{xx}}n_e, \tag{66}$$

which can serve as a boundary condition (the left side in the above equation is $j_x(x = 0)$). This boundary condition relates the charge accumulation n_e to the normal component of the current at the edge. A Green function approach can be used to solve the above equation [6]. We define a Green function as

$$\left(\frac{\partial^2}{\partial x^2} - q^2\right)G(x, x') = -\delta(x - x') \tag{67}$$

valid for $x, x' < 0$ and subject to the following boundary condition

$$\left[\left(\frac{\partial}{\partial x} + iq\frac{\sigma_{xy}}{\sigma_{xx}}\right)G(x, x')\right]_{x=0^-} = 0, \tag{68}$$

assuming the above homogeneous boundary condition at $x = 0^-$, a bounded response at $x \to -\infty$, and the following jump condition at $x = x'$,

$$\left(\frac{\partial G(x, x')}{\partial x}\right)_{x=x'^+} - \left(\frac{\partial G(x, x')}{\partial x}\right)_{x=x'^-} = -1. \tag{69}$$

The solution for the Green function is

$$G(x, x') = \frac{\sigma_{xx} - i\sigma_{xy}}{2q(\sigma_{xx} + i\sigma_{xy})}e^{q(x+x')} + \frac{1}{2q}e^{-q|x-x'|}, \tag{70}$$

and using Green's second theorem the potential can be obtained as

$$\begin{aligned} \phi(x) = &-\frac{ie\omega}{\sigma_{xx}}\int_{x'=-\infty}^{0} G(x, x')n_b(x')dx' \\ &+ G(x, 0)\left[\left(\frac{\partial}{\partial x} - iq\frac{\sigma_{xy}}{\sigma_{xx}}\right)\phi(x)\right]_{x=0}. \end{aligned} \tag{71}$$

The edge charge accumulation in Eq. (66) is in terms of $\phi(x = 0)$ and $\partial_x\phi|_{x=0}$. These parameters can be found using the above equation as

$$\begin{aligned} \phi(0) = \Bigg(&-\frac{ie\omega}{\sigma_{xx}}\int_{x'=-\infty}^{0} G(0, x')n_b(x')dx' + \\ &G(0, 0)\left[\frac{\partial\phi}{\partial x}\right]_{0^-}\Bigg) \times \left[1 - iq\frac{G(0, 0)\sigma_{xy}}{\sigma_{xx}}\right]^{-1} \end{aligned} \tag{72}$$

$$\begin{aligned} \left[\frac{\partial\phi(x)}{\partial x}\right]_{x=0} = \Bigg(&-\frac{ie\omega}{\sigma_{xx}}\int_{x'=-\infty}^{0}\frac{\partial G(x, x')}{\partial x}n_b(x')dx' \\ &+ \left(\frac{\partial G(x, 0)}{\partial x}\right)_{x=0} iq\frac{\sigma_{xy}}{\sigma_{xx}}\phi(x = 0)\Bigg) \\ &\times \left[1 - \left(\frac{\partial G(x, 0)}{\partial x}\right)_{x=0}\right]^{-1} \end{aligned} \tag{73}$$

and simultaneously solving equation 72 and 73 for $\phi(x = 0)$ and $\partial_x\phi|_{x=0}$ gives

$$\left[\frac{\partial\phi(x)}{\partial x}\right]_{x=0} = \frac{1}{\alpha\gamma - XG(0,0)}\left(\frac{-ie\omega}{\sigma_{xx}}\right)\int_{x'=-\infty}^{0}\left[\alpha\left(\frac{\partial G(x,x')}{\partial x}\right)_{x=0} + XG(0,x')\right]n_b(x')dx' \tag{74}$$

$$\phi(x=0) = \frac{-ie\omega}{\sigma_{xx}}\int_{x'=-\infty}^{0}\left[\left(\frac{1}{\alpha} + \frac{G(0,0)X}{\alpha\left(\alpha\gamma - XG(0,0)\right)}\right)G(0,x') + \frac{G(0,0)X}{\alpha\gamma - XG(0,0)}\left(\frac{\partial G(x,x')}{\partial x}\right)_{x=0}\right]n_b(x')dx' \tag{75}$$

where

$$\alpha = 1 - G(0,0)iq\frac{\sigma_{xy}}{\sigma_{xx}},\quad \gamma = 1 - \left(\frac{\partial G(x,0)}{\partial x}\right)_{x=0}$$
$$X = \left(\frac{\partial G(x,0)}{\partial x}\right)_{x=0} iq\frac{\sigma_{xy}}{\sigma_{xx}}. \tag{76}$$

Inserting $\phi(x=0)$ and $\partial_x\phi|_{x=0}$ in (66) gives n_e in terms of the Green function as

$$n_e = \int_{x'=-\infty}^{0}\left[\left(A\alpha + Biq\frac{\sigma_{xy}}{\sigma_{xx}}\right)\frac{a-1}{2}e^{qx'} + \left(AX + Ciq\frac{\sigma_{xy}}{\sigma_{xx}}\right)\frac{a+1}{2q}e^{qx'}\right]n_b(x')dx', \tag{77}$$

where

$$a = \frac{\sigma_{xx} - i\sigma_{xy}}{\sigma_{xx} + i\sigma_{xy}},\quad A = \frac{1}{\alpha\gamma - XG(0,0)}$$
$$B = \frac{XG(0,0)}{\alpha\gamma - XG(0,0)},\quad C = \frac{1}{\alpha} + \frac{G(0,0)X}{\alpha\left(\alpha\gamma - XG(0,0)\right)}. \tag{78}$$

It is shown below that the potential satisfies the integro-differential equation

$$\phi(x,z=0) = -\frac{e}{\epsilon_0}\int_{x'=-\infty}^{0}dx'L(x,x')n_b(x') - \frac{e}{\epsilon_0}L(x,0)n_e \tag{79}$$

where

$$L(x,x') = \int_{k=-\infty}^{+\infty}\frac{dk}{2\pi}\frac{e^{ik(x-x')}}{2\sqrt{k^2+q^2}}. \tag{80}$$

Alternatively, one may use the approximate expression $L_0(x,x') = 2^{-3/2}e^{-\sqrt{2}q|x-x'|}$[4, 7]. Replacing the potential by the expression of potential in Eq. (71) gives

$$\frac{i\omega\epsilon_0}{\sigma_{xx}}\int_{x'=-\infty}^{0}G(x,x')n_b(x')dx' - \int_{x'=-\infty}^{0}dx'L(x,x')n_b(x') + \left(G(x,0)\frac{i\omega\epsilon_0}{\sigma_{xx}} - L(x,0)\right)n_e = 0, \tag{81}$$

where n_e (charge accumulation at the edge) is given by Eq. (77). We expand the bulk charge fluctuation n_b in terms of Laguerre polynomials [3, 8]

$$n_b = \sum_{j=0}^{\infty}b_j e^{qx}l_j(-2qx) \tag{82}$$

subject to the orthogonality relation

$$\int_{x=-\infty}^{0}(e^{qx}l_i(-2qx)) \times (e^{qx}l_j(-2qx))dx = \frac{\delta_{ij}}{2}. \tag{83}$$

The integral equation in (81) can be written in a matrix form in terms of unknown constants b_j and n_e,

$$\sum_{j=0}^{\infty}\left[\frac{i\omega\epsilon_0}{\sigma_{xx}}G_{ij} - L_{ij} + Ne_{ij}\right]b_j = 0 \tag{84}$$

where

$$
\begin{aligned}
G_{ij} &= \int_{x=-\infty}^{0}\int_{x'=-\infty}^{0} dxdx' e^{qx}e^{qx'} l_i(-2qx)G(x,x')l_j(-2qx') \\
L_{ij} &= \int_{x=-\infty}^{0}\int_{x'=-\infty}^{0} dxdx' e^{qx}e^{qx'} l_i(-2qx)L(x,x')l_j(-2qx') \\
Ne_{ij} &= \int_{x=-\infty}^{0}\int_{x'=-\infty}^{0} dxdx' e^{qx}e^{qx'} l_i(-2qx)\Lambda\left(\frac{i\omega\epsilon_0}{\sigma_{xx}}\frac{a+1}{2q}e^{q(x+x')} - L(x,0)e^{qx'}\right) l_j(-2qx') \\
\Lambda &= \frac{a-1}{2}\left(A\alpha + Biq\frac{\sigma_{xy}}{\sigma_{xx}}\right) + \frac{a+1}{2q}\left(AX + Ciq\frac{\sigma_{xy}}{\sigma_{xx}}\right).
\end{aligned} \tag{85}
$$

Finally, forcing the determinant of (84) to be zero leads to the edge mode dispersion equation.

Derivation of IE: The Poisson's equation considering edge mode propagating along the y-axis as $e^{iq_y y}$, $q_y = q$, is

$$
\left(\frac{\partial^2}{\partial x^2} + \frac{\partial^2}{\partial z^2} - q^2\right)\phi = \frac{ne}{\epsilon_0}\delta(z)\Theta(-x), \tag{86}
$$

and taking a Fourier transform along the x-axis leads to

$$
\left[\frac{\partial^2}{\partial z^2} - \left(k^2+q^2\right)\right]\phi = \frac{e}{\epsilon_0}\delta(z)n(k), \tag{87}
$$

where $n(k)$ is the Fourier transform of $n\Theta(-x)$. The potential takes the form

$$
\phi(k,z) = -\frac{e}{2\epsilon_0}\int_{x'=-\infty}^{0} n(x')e^{-ikx'}dx' \frac{1}{\sqrt{k^2+q^2}} e^{-\sqrt{k^2+q^2}|z|}. \tag{88}
$$

By defining the function kernel $L(x)$ as

$$
L(x) = \int_{k=-\infty}^{+\infty} \frac{dk}{2\pi}\frac{e^{ikx}}{2\sqrt{k^2+q^2}}, \tag{89}
$$

then the potential function on the surface of the 2D electron fluid becomes

$$
\phi(x, z=0) = -\frac{e}{\epsilon_0}\int_{x'=-\infty}^{0} dx' L(x-x')n(x'). \tag{90}
$$

Replacing $n(x)$ by $n_b(x) + n_e\delta(x)$ gives

$$
\begin{aligned}
\phi(x,z=0) = &-\frac{e}{\epsilon_0}\int_{x'=-\infty}^{0} dx' L(x,x')\left[n_b(x') + n_e\delta(x')\right] \\
&-\frac{e}{\epsilon_0}\int_{x'=-\infty}^{0} dx' L(x,x')n_b(x') - \frac{e}{\epsilon_0}L(x,0)n_e,
\end{aligned} \tag{91}
$$

and substituting n_e from the boundary condition equation leads to (79).

[1] M. Gajdoš, K. Hummer, G. Kresse, J. Furthmüller, and F. Bechstedt, *Linear optical properties in the projector-augmented wave methodology*, Phys. Rev. B **73**, 045112 (2006).

[2] V. P. Gusynin, S. G. Sharapov, and J. P. Carbotte, *Magneto-optical conductivity in graphene*, J. Phys.: Condens. Matter **19**, 026222 (2007).

[3] W. Wang, P. Apell, and J. Kinaret, *Edge plasmons in graphene nanostructures*, Phys. Rev. B **84**, 085423 (2011).

[4] A. L. Fetter, *Edge magnetoplasmons in a bounded two-dimensional electron fluid*, Phys. Rev. B **32**, 7676 (1985).

[5] W. Wang, J. Kinaret, and P. Apell, *Excitation of edge magnetoplasmons in semi-infinite graphene sheets: Temperature effects*, Phys. Rev. B **85**, 235444 (2012).

[6] G. W. Hanson and A. B. Yakovlev, *Operator Theory for Electromagnetics: An Introduction*, Springer, New York (2002).

[7] D. B. Mast, A. J. Dahm, and A. L. Fetter, *Observation of bulk and edge Magnetoplasmons in a two-dimensional electron fluid*, Phys. Rev. Lett. **54**, 1706 (1985).

[8] X. Xia and J. J. Quinn, *Multipole edge plasmons of two-dimensional electron-gas systems*, Phys. Rev. B **50**, 8032 (1994).